Paper-31

Facile Synthesis and Characterization of Copper Oxide (CuO) Nanoparticles via Sol-Gel Method.

Sangita Shinde[1], Pallavi Nalle[2], P. Kute[3], Firdos Quadri[4*] and N. D. Chaudhari[5]

[1,3, 4]Department of Physics, Pratishthan Mahavidyalaya, Paithan, Aurangabad, M.S. India.

[2]Department of Physics, Shri Shivaji Science and Arts College, Chikhali, Dist. Buldana, M.S. India, ***[4*]****Dr.Rafiq Zakaria College for Women, Aurangabad, M.S. India.*

Abstract

Metal and metal oxide particles are very importance because of their prominence in different fields of applications in Science and Technology. In this present paper work Copper Oxide (CuO) Nanoparticles are synthesized by Sol-Gel technique in ethanol media. Copper Chloride ($CuCl_2$) was used to prepare Copper Oxide Nanoparticles. The synthesized nanoparticles are characterized by using X-ray powder diffractometry (XRD) to find the crystallinity, UV- visible spectra and Scanning Electron Microscope (SEM). The XRD data reveals that the prepared CuO-nanoparticles are pure, crystalline and nano-sized. The SEM image suggested that CuO nanoparticles are like rice grains or needle shape and there is a tendency of agglomerations. UV-visible spectra gives the band gap of nanoparticle CuO which is 3.43 eV after calculation. Nanoparticles shows the interaction between Copper and Oxygen. This method is more economical, convenient, easy and effective in comparison to other known methods of synthesis of nano-materials.

Keywords

Copper Oxide Nanoparticles; Chemical Precipitation; Nanotechnology; *Sol-Gel*; *X-ray Diffraction*; *SEM*.

---

1. INTRODUCTION

Over the last decade, transition metals and metal oxide are numerous applications in different fields. Nowadays metal oxide nanomaterials have attracted researchers due to their unique

physical and chemical properties that makes them technologically very important in numerous fields [1, 2]**.** Copper Oxide (CuO) is one of useful metal oxide which has numerous applications in range fields. Copper oxide nanoparticles have a great efficiency as Nanofluids in heat transfer applications. Some Scientist has been reported that by just 4% addition of CuO increases the thermal conductivity of water by 20% [3]**.** Copper Oxide has a semiconducting compound with a narrow band gap. It has used for photoconductive and photothermal applications.

Copper oxide nanoparticles has various applications such as gas sensors, magnetic storage media, batteries, semiconductors, solar energy transformation and field emission…etc [4,5]**.** The numerous methods are used to prepare copper oxide nanoparticles, including solid state reaction, sol-gel, sonochemical preparation, microwave irradiation, alkoxidebased synthesis and thermal decomposition [6,7]. In the present work, for the synthesis of nano particles of copper oxide sol-gel method was used as it was more economical, faster and easier.

2. EXPERIMENTAL

2.1. *Materials.*

Analytical Reagent (AR) grade chemicals such as Copper chloride (II) $CuCl_2$, Sodium hydroxide NaOH, Acetone and Ethanol C_2H_5OH were used as starting material for the synthesis of CuO. These chemical were purchased from Merck with purity 99.9%. These chemicals were used as purchased without further treatment in this study.

2.2. *Synthesis of CuO*

For synthesis of CuO-NPs, at first 6.0 g of copper (II) chloride dehydrate was dissolved in 320 ml of Ethanol and 3.6 g of sodium hydroxide pellet were dissolved in 100 ml ethanol separately. Drop wise addition of sodium hydroxide solution to copper (II) chloride dehydrate solution was carried out with constant stirring at room temperature. The color of the solution was turned from green to bluish green and finally to black as the reaction proceeded. The black precipitate was copper hydroxide. The precipitate was filtered by a centrifuge (Eppendorf Refrigerated Centrifuge Model 5702R, Germany). Then washed with ethanol and deionized water to remove the sodium chloride salt solution. After that, the precipitate was dried at about 50˚C in the dryer. The dried sample was annealed at temperature 100˚C to obtain crystalline CuO-NPs. Then the annealed sample was grinded to get the powdered nanoparticles. The powder sample was used to characterize CuO-NPs. Schematically the chemical reaction can be represented as:

$$CuCl_2 + 2NaOH \rightarrow CuO + 2NaCl + H_2O$$

2.3 Characterization Techniques

The prepared sample of copper oxide nano particle was characterized by XRD i.e. X-ray diffraction technique The crystalline structure, phase composition and crystallite size of CuO were revealed from XRD patterns obtained using Cu Kα radiation (λ = 1.541 Å) for 2θ value ranging from 10o to 60o in X-ray diffractometer (Bruker AXS D8 Advance). The morphology of the particles is observed by a scanning electron microscope (SEMEDS) using SEM make JEOL Model JSM - 6390LV and EDS make JEOL Model JED – 2300 with an accelerating voltage of 20 kV.

3. RESULTS AND DISCUSSION

3.1 X-Ray Diffraction Analysis

The crystal structure and phase purity of the nanoparticles were characterized by XRD. Fig. 1. Shows the XRD pattern of CuO nanoparticles. The XRD diffractogram of CuO nanopowder shows diffractions peaks at 31.7º, 34.7º, 38.0º, 47.9º, 52.7º, 57.5º, correspond to (110), (002), (111), (202), (020) and (113) reflections of CuO [8]. All the peaks can be indexed to the monoclinic crystal system CuO. The XRD patterns confirmed the synthesis of pure crystalline copper oxide nanoparticles.

Average crystallite size has been estimated from the XRD pattern using the Scherrer's equation [9-10].

$$D = K\lambda / \beta \cos\theta \qquad (1)$$

Where K is a constant (0.9); λ is the X-ray wavelength used in XRD (0.15405 nm); θ is the Bragg angle; β is the FWHM (full width at half maximum intensity), that is, broadening due to the crystallite dimensions. The average crystallite size of CuO nanoparticles is found to be around 19.48 nm.

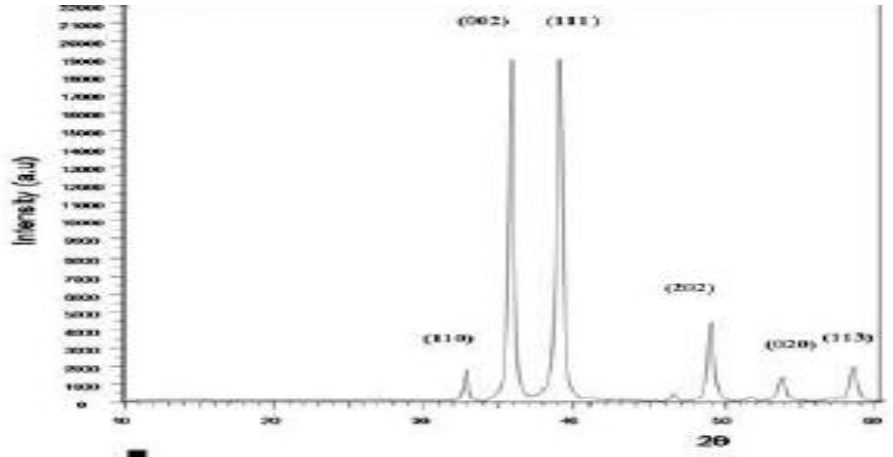

Fig. 1. XRD Spectra of CuO Nanoparticles

3.2 ***Scanning Electron Microscopy (FE-SEM)***

The morphology of copper oxide nanoparticles was examined by SEM. Fig. 2. Shows the SEM micrograph of the CuO nanoparticles at 15,000X magnification. It was apparent from SEM image that copper oxide nanoparticles were needle shape. The SEM micrographs revealed little aggregates of chemically synthesized nanoparticles[11].

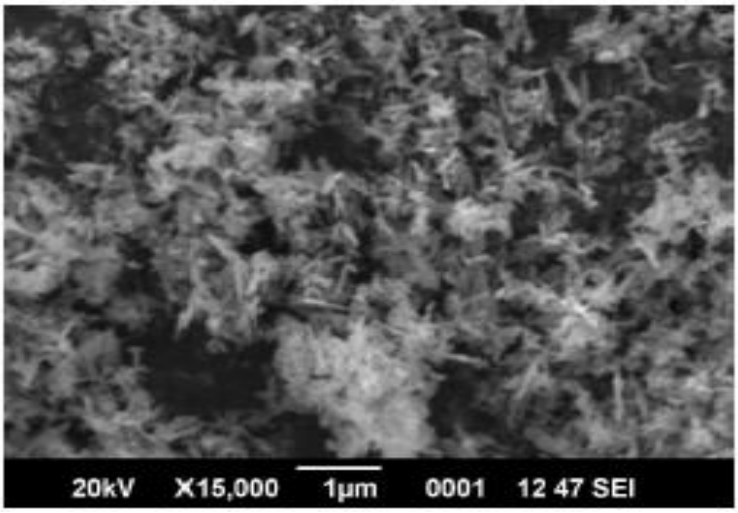

Fig. 2. SEM Micrograph of CuO Nanoparticles

4. CONCLUSION

In this paper nontoxic, versatile and environmental friendly approach for the synthesis of copper oxide nanoparticles is presented. CuO nanoparticles were successfully synthesized by sol-gel auto combustion method. XRD pattern revealed that copper oxide nano particles have monoclinic structure as well as pure phase formation of copper oxide with no impurities. The average crystallite size of the prepared sample was found to be 19.48 nm. SEM micrograph shows that shape of CuO nanoparticles was needle shape. This facile, low cost approach and reproducible should promise us a future large scale synthesis of nanostructures for many applications in nanotechnology.

REFERENCES

1. S.Gubbala, H.Nathani, K.Koizol, R.D.K. Misra, Physica B, 348 (2004) 317-28
2. P.Pramanik, Bull. Mater. Sci., (1995) 335
3. W.Wang, Y.Qi, Y.Ma, X.Li, X.Guo, J.Gao, M.Chen, Mater. Chem. Phys., 36 (2004)192
4. J. Azadmanjiri, S.A.Seyyed Ebrahimi, Phys. Stat. Solidi © 1 (2004) 3414
5. S.A.Khorrami, N.Naderfar, M.G.G. Mojadad, A.Z.Asian and R.Lotfi, J.Phys and Theo. Chem., 7(2) 91-94, Summer 2010
6. D.A.Sumo, m.R.Morelli, A.m. Segadaes, Mater. Res. Bull., 31 (1996) 1243.
7. AL Patterson, Phys. Rev., 1939, 56, 978.
8. S.Bajaj, P Patil, G N Kakade, S D Tapsale, K M Jadhav, S Shinde*, J.Phys: conference series 1644(2020) 012022
9. Shakti Bajaj, A.V.Raut, M.V. Khedkar, Sangita Shinde, K.M. Jadhav, AIP Conference proceeding 2369, 020182(2021) 13 sep. 2021 online publish.
10. M Rashad; M Rüsing; G Berth; K Lischka; A Pawlis, J. Nanomater., 2013, 2013, Article ID 714853, 6 pages.
11. Rajgovind; G Sharma; D Gupta Kr; ND Jasuja; SC Joshi, J. Microb. Biochem. Technol., 2015, 7, 140.

Paper-32

Study of Exposure Dose of Gamma Radiations on Output Response of Silicon Solar Cell Panel.

Sukhada Pande, G.R.Pansare
Department of Physics, Haribhai V. Desai College, Pune

Abstract

Present research paper reports the effects of gamma radiations on output response of solar cell panel. The output response is measured in terms of light conversion efficiency of 3 watt silicon solar cell panel. In the present work solar panel was exposed to gamma radiations of standard radioactive sources Co-60, Cs-137, Na-22.The solar panel was kept under the intensity of 330 watt/m². All the external parameters such as environmental temperature, intensity etc. were kept constant. The gamma radiation exposure dose was varied in the range of 12.42×10^8gamma rays to 124.2×10^8gamma rays. Gamma radiation exposure dose was also measured using the NaI(Tl) gamma ray spectrometer. For every dose the parameters of exposed solar panel such as short circuit current, open circuit voltage, fill factor and conversion efficiency were measured. The results indicate that the average value of light conversion efficiency of solar panel was increased from 14.85% to 16.25% up to the exposure dose of 12.42×10^8 gamma rays and there after the increase in the value of efficiency is found to be almost constant up to the exposure dose of 124.2×10^8 gamma rays.

Introduction:

Silicon solar cells are introduced in 1955, There are two types of silicon solar cells, mono crystalline and polycrystalline. The solar cells work on solar energy which is a clean and green source of energy. These silicon cells are commercially used in smaller as well as on larger scale as per needed. Crystalline solar cells get affected by the external environmental parameters. As the efficiency of the solar cell panel is an extremely important factor regarding the quality of the solar panel. Researchers all over the world are taking efforts in this direction to increase the efficiency of solar cell panel. In view of this efforts have been taken to improve the efficiency of silicon solar cells panel by exposing it to the gamma radiations.

Experimental Details:

In the present work, silicon solar cell panel of 3 watt having 36 solar cells of area 19.44×10^{-3} m^2 is used. Various parameters such as open circuit voltage, short circuit current, maximum current, maximum voltage, fill factor and light conversion efficiency of silicon solar cell were measured before the exposure of gamma radiations. Experiment was repeated three times with all the experimental condition keeping constant, throughout the experiment, the intensity of light of 330 W/m^2 was kept constant and monitored using sunmeter. The average value of light conversion efficiency was calculated and confirmed.

Solar cell panel was exposed to the gamma radiations obtained from standard gamma ray sources Cs-137,Na-22 and Co-60 for different exposure dose in the range of 12.42×10^8 to 124.2×10^8 radiations. The total energy dose was calculated from the gamma rays of energy 662KeV (Cs-137) ,511KeV and 1275KeV (Na-22) and 1170KeV and 1330KeV (Co-60) sources. Gamma radiation exposure dose was measured using the NaI(Tl) scintillation spectrometer and 8K multichannel analyzer from the observed gamma radiation photo peaks. Standard relations were used to calculate the exposure dose of gamma radiations. Output parameters of solar cell panel such as maximum output power, fill factor, efficiency, short circuit current, open circuit voltage were measured after every exposure dose of gamma radiations.

Table 1 gives measured efficiency with variation of gamma radiation dose.

Figure 1 gives the gamma rays spectrum of Cs-137, Co-60 and Na-22 gamma rays sources recorded using NaI(Tl) gamma ray spectrometer.

Figure 2 shows the variation of light conversion efficiency of solar cell panel with gamma radiation exposure dose.

Table 1 : Measured light conversion efficiency with variation of gamma radiation dose

Exposure Period (Hours)	Exposure Period (Second)	Gamma Radiations Exposure Dose (Radiations)	Gamma Radiations Energy Dose (KeV)	Efficiency of Solar cell Panel (%)
0	0	Nil	Nil	14.85%
3	10800	12.42×10^{8}	11.4×10^{11}	16.25%
6	21600	23.96×10^{8}	22.22×10^{11}	16.16%
9	32400	36.94×10^{8}	33.4×10^{11}	16.83%
10	36000	41.2×10^{8}	37.75×10^{11}	16.51%
12	46800	53.28×10^{8}	49.08×10^{11}	16.91%
15	54000	61.8×10^{8}	58.8×10^{11}	16.50%
18	64800	73.4×10^{8}	67.43×10^{11}	16.56%
21	75600	86.88×10^{8}	79.79×10^{11}	16.49%
24	86400	99.45×10^{8}	91.26×10^{11}	16.07%
27	97200	111.88×10^{8}	102.72×10^{11}	16.44%
30	108000	124.2×10^{8}	114.04×10^{11}	16.16%

Figure 1 : Gamma rays spectrum of Cs-137, Co-60 and Na-22 gamma rays sources recorded using NaI(Tl) gamma ray spectrometer

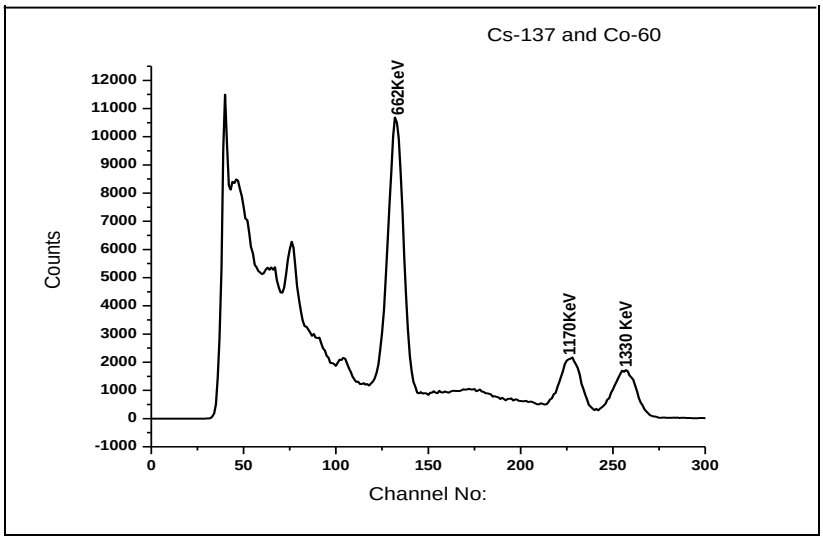

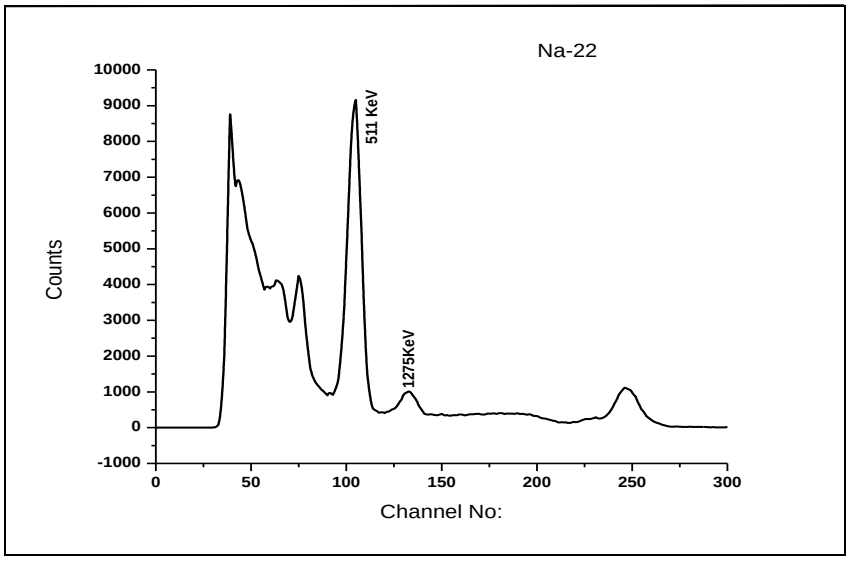

Figure 2 : Light conversion efficiency of solar cell panel with variation of gamma radiation exposure dose.

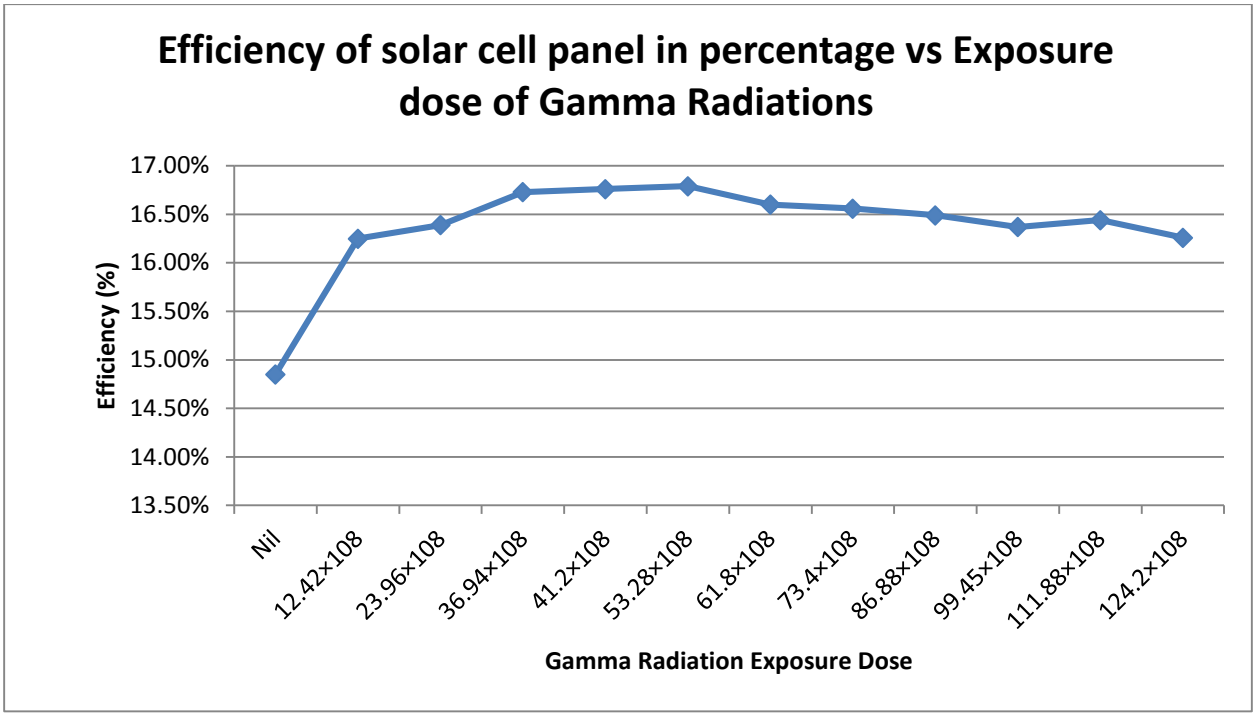

Results and Conclusions

The gamma radiations exposure dose was varied in the range of 12.42×10^8 gamma rays to 124.2×10^8 gamma rays. The result indicates that the average value of light conversion efficiency of solar cell panel was increased from 14.85% to 16.25% up to the exposure dose of 12.42×10^8 gamma rays and thereafter the value of efficiency is found to be almost constant up to an exposure dose of 124.2×10^8 gamma rays.

Acknowledgement

Authors are thankful to the Haribhai V. Desai College for partial financial support. Authors are also thankful to the principal Dr. Girish Pathade and P.G.K. Mandal for cooperation.

References

1. A.D.Neaman, “Semiconductor Physics and Device”,MacGraw Hill,2003.

2. C.S.Solanki, “Solar Photovoltaics”, PHI Learning, 2013.

3. D.C.Tayal. “Nuclear Physics”, Himalaya Publishing House, 2009.

Paper-33

"SYNTHESIS OF NANOCRYSTALLINE ZIRCONIA BY VARIOUS CHEMICAL METHODS : REVIEW"

Tejas C. Gaikwad
Dept. of Chemistry, M.J.M. Arts, Commerce and Science College Karanjali (Peth),
Nashik. M. S., India,

Abstract:

Zirconium oxide nanoparticles are having major applications in research & industries due to its different & multifunctional aspects, industrial applications. The Last decades study showed that zirconia nanoparticles were synthesized by various chemical methods due to its wide applications & high demand in practical use like amorphous nanocrystalls, nano thin films, nanopowders, nanao-rods, nano-solarcells, electronics, optics, nanocomposites, in surface coating technology,etc.`ZrO2 nanocrystals were synthesized by the microwave combustion method (MCM), conventional combustion method (CCM), Microwave irradiation Method, chemical co-precipitation method, sol-gel method and Hydrothermal method . By using thermal treatment ZrO2 nanoparticles also prepared by this ecofriendly method.In present article we have reported different deposition techniques employed by Various researchers.

Keywords: Zirconia, Nanocrystals, thin films, nanocomposites.

Introduction:

Zirconium Oxide nanoparticles have attracted scientific attention due to their Wide band gap and wide range applications. Zirconium oxide (ZrO2) also known as zirconia with its excellent chemical and physical properties have applications such as fuel cells [1], gas sensors [2], optoelectronics [3], catalyst [4], and corrosion resistant material [5]. With band gap >5 eV, ZrO2 is an important luminescent material with good optical transparency [6] and a potential candidate for photocatalytic applications due to its high surface area and large number of oxygen vacancies presen in it [7]. It comes in three crystal phases namely tetragonal, monoclinic and cubic. The existence of these polymorphs depend on the synthesis process, particle size, calcination temperature and defects. There are contrasting reports on the existence of the phases with calcination temperature. Although monoclinic ZrO2 is believed to be more stable at room temperature than the other two polymorphs but the tetragonal phase can also be stabilized at

room temperature depending on the synthesis process [8]. In literature there exist various methods of synthesis of ZrO2 nanostructures like sol-gel [9], hydrothermal [10], combustion [11], and co-precipitation [12-13].

Result and Discussion:

V. Santos et. al.[14] obtained nanostructured zirconia powders by sol–gel process. Obtained structure of the zirconia produced was amorphous with the monoclinic phase, resulting in the lowering of the content of tetragonal phase. The thermogravimetric analysis showed a considerable weight loss between 40°c and 200 °C, which was due to dehydration. An exothermic peak followed by a weight loss at approximately 450 °C is observed, which was a typical behavior related to the combustion of organic compounds. At a temperature higher than 450 °C, another exothermic peak was observed, but not followed by any weight loss, attributed to the allotropic transformation of zirconia from tetragonal to monoclinic, which was confirmed by X-ray diffraction. The water loss was confirmed in the spectrum FTIR. It was observed that the formation of the bands related to the presence of hydroxyl group showed a decrease with the increase of annealing temperatures, and at 800 °C they disappeared, showing that the material structure no longer contains zirconium hydroxide. The crystallite size (estimated by both TEM and XDR single-line method) increases with increasing annealing temperatures: it was approximately 20–25 nm for monoclinic phase and 17–28 nm for tetragonal phase after annealing at temperatures of 700 and 800 °C, respectively. The so-obtained zirconia powders presented as micrometer-sized agglomerates (mean particle size of 11.54 μm). The tetragonal phase was stable at 500°C because of the reduction of the surface energy, which was caused by small-sized crystallites. Masoud Salavati et.al. [15]successfully obtained Pure zirconium oxide nanocrystals by thermal decomposition method. They were used SEM,TEM, XRD and XPS techniques to characterize the structure of zirconia nanocrystals . XRD analysis indicated that the nanoparticles closely resembled and had the cubic zirconia nanocrystals. From the results of UV–Visible absorption spectrum and FT-IR bsorption spectrum, it was cleared that cubic ZrO2 phase was favored for technological advanced optical applications including on transparent optical devices, optical fiber connector and photocatalysis compared by monoclinic ZrO2. H.S. Chen et.al.[16] suggested that Pyrochlore lanthanum zirconium oxide thin films textured along (400)have been fabricated using lanthanum acetate hydrate,zirconium propoxide, propionic acid,

acetic acid glacial, and methanol as precursors. Annealed LZO films composed of nanocrystallites sizing 10–15nm have a dense and smooth structure and rare pinholes sizing 25–35 nm. The formation of the LZO films was based on the decomposition of a mixture of La and Zr solution. Zr metal–oxide bonds were found to be first eliminated at around 250 ◦C that leads to the formation of a gel. Subsequent annealing at 900 ◦C for an hour caused the compounding and the formation of LZO film in the presence of carboxylates. The process was identified as a solution–gel process. Sadok Letaief et.al.[17]got the remarkable structural features of the clay mineral sepiolite were used to prepare an efficient catalyst for the Knoevenagel condensation of benzaldehyde derivatives under solvent-free conditions. An inorganic nanocomposite was prepared by the deposition of zirconium oxide nanoparticles on the external surfaces of sepiolite. The nanoparticles were prepared by a sol–gel technique, from solutions of zirconium(IV) propoxide in 1-propanol as precursor. After calcination at 650º C, the organic material from the precursor was lost, the coordinated water of sepiolite was fully removed, and the layered structure of sepiolite was folded. However, the arrangement of the nanoparticles of zirconium oxide on the external surfaces maintains a fibrous morphology for the nanocomposite. These modifications, which take place at the nanometer scale under soft conditions, produce a functional nanocomposite material combining the textural properties of the pristine clay mineral and the catalytic activity of zirconium oxide.The material was applied to the solvent-free reaction of the condensation of benzaldehyde and malononitrile. The condensation reaction, which necessitates mild basic conditions, Was there governed by the porosity of the supporting sepiolite (increasing the density of supported nanoparticles) and the basicity and catalytic effect of the ZrO2 nanoparticles. Strongly improved yields of reaction, attributed to larger catalytically active surfaces, were obtained in the case of the inorganic nanocomposite material, compared with either the sepiolite mineral or the zirconium oxide tested individually. MRH Siddiquia et.al. [18] have obtained Pure zirconium oxide nanoparticles were successfully prepared by sol-gel method. Using this method zirconia nanopatricles were synthesized in non-aqueous medium. The results clearly indicate that the morphology and size of ZrO2 nanoparticles was highly dependent on the precursor used. XRD analysis indicated that the nanoparticles closely resembled and had the tetragonal and monoclinic zirconia nanocrystals. The crystallite size for ZrOCl2 precursor was estimated to be 18.1 nm and that from Zr(SO4)2.H2O was 9.7 nm. The TEM results show very different size and shapes for the nanoparticles obtained from the two different precursors. Qi Li

et.al. [19] Repoted a low-cost, simple method for the synthesis of am-ZrO2 nanoparticles which had good arsenic removal performance and the potential industrial applicability. The material was chemical stable, inexpensive (compared with its commercially available counterparts), and non-toxic. The adsorption process was effective under near neutral pH environment and required no pretreatment of oxidation/pH adjustment. Am-ZrO2 nanoparticles demonstrated an effective removal performance on both As(III) and As(V) in either lab-prepared or natural water samples. The adsorption capacities of these am-ZrO2 nanoparticles on As(III) and As(V) at pH 7 are 83.2 mg/g and 32.5 mg/g, respectively. The adsorption mechanism of arsenic species onto am-ZrO2 nanoparticles was determined to follow the inner-sphere complex mechanism. With only a relatively low material loading concentration (0.1 g/L), these am-ZrO2 nanoparticles successfully removed most of the arsenic contamination from natural water samples of Lake Yang zonghai to meet the MCL for drinking water. am-ZrO2 nanoparticles immobilized on glass fiber cloth showed an even better removal effect than am-ZrO2 nanoparticles dispersed in water, which reduces the possible dispersion of nanoparticles into the environment and was critical to their potential applications in the real practice. Thus, it may provide a simple single step treatment option to treat arsenic contaminated natural water, which requires no pretreatment or post-treatment pH adjustment and could largely lower the cost and the pollution risk from adding large amount of chemicals into natural water bodies. Further work was now underway to immobilize them onto various substrates, to test their continuous treatment of arsenic-bearing water in flow through reactors, and to develop effective desorption and regeneration process.

J. Judith Vijaya et.al. [20] have successfully synthesized ZrO2 nanocrystals by simple and rapid MCM and ZrO2 micro-crystals by CCM using urea as the fuel. In comparison with CCM, MCM was not only a quick processes, but also uniformly spreads the heat through the entire bulk of the reaction mixture, which result in the formation of a nanospherical structure with a narrow distribution of particle size. Both MCM and CCM rendered ZrO2 to crystallize rapidly, assisting in the inclusion of crystal defects. However, MCM could be an effective and convenient alternate method to produce ZrO2 nanocrystals, which enhances the photocatalytic degradation of 4-CP. ZrO2–TiO2 mixed oxide catalysts were tested for the photocatalytic degradation of 4-CP, and the ZrO2–TiO2 mixed oxides showed activity that was comparable to the activity of pure TiO2. Therefore, MCM methodology may promote the control of desired morphologies of functional oxide materials for optical and photocatalytic applications. R.

Madhusudhanaet.al. [21] have synthesized ZrO2 powder starting from Zirconium alkoxide as precursor and acetic acid as chelating agent using sol-gel method. The resulting zirconia powders were characterized by X-ray diffraction, and scanning electron microscopy (SEM). Applying a heat treatment at temperatures higher than 700 oC leads in obtaining crystalline zirconia as single phase (monoclinic). Using sol-gel method and heat treatment at 700º C for one hour zirconia powder of crystallite size 25.39 nm was obtained, both for the inorganic and organic precursor . Zirconia powders obtained at the nanometric scale may have superior properties as compared to the powders of other ceramics and can be used extensively used for thermal shielding since it has very high resistance to crack propagation. Wei Jiang et.al. [22] Reported zirconium foil was anodized in electrolyte containing 1M $(NH4)_2SO_4$ and 0.25 wt.% NH_4F to in situ construct the zirconia nanotubes on the surface. The final ZNT product was analyzed and applied as photocatalyst to degrade MO solution under UV irradiation. After anodization for 120 minutes at 20 V, ZNT with a diameter of 20 nm, thickness of 5 nm and length of 600 nm was built to form an order tubes array layer on the surface of Zn foil. The as-grown ZNT was the mixed crystal of monoclinic and tetragonal ZrO2 and transformed into pure monoclinic structure after annealed at 300 ºC. The growth hypothesis of ZNT that the initial etching occurred at the defects of the Zr foil surface was confirmed. With the processing of anodization, the etched pits further deepened to in situ form nanotubes. On the rough surface with ripples, the tubes firstly grew at the bottom and finally to construct intensive but disordered tube rundles. ZNT has equivalent photocatalytic performance compared with TiO2 nanotubes in photo-degradation process of MO. The top degradation rate reached 94.45% after 240 minutes, and the speed was faster than TiO2 in the early stage. This photocatalysis performance should be ascribed to the hydroxyl group absorbing on the surface. The stability of ZNT was good for reusing as photocatalyst. After 6 recycling, the degradation rate almost kept constant if no mechanical destruction. Das et.al. [23]ZrO2 nanoparticles were synthesized using the hydrothermal method. The composition of ZrO2 nanoparticles was deepstated by X-ray diffraction (XRD). By using scanning and transmission electron microscopy (SEM and TEM) the size and the morphology of the samples were characterized. The size of the ZrO2 nanoparticles was distinguished using transmission electron microscopy (TEM), which also helped to determine the size of the prepared ZrO2 nanoparticles and the particle size was found to be &24 nm. The FT-IR spectrum demonstrated the strong existence of ZrO2 nanoparticles. The optical properties were examined by the UV–Vis

absorption spectrum. The band gap valuewas found to be 5.02 eV.Room temperature photoluminescence demonstrated intrinsic defects of oxygen vacancies. The optical property of the prepared ZrO2 nanoparticleswas examined by PL study and it exhibited the oxygen vacancies accompanied intrinsic defects. The dielectric constant and the dielectric loss were examined at different temperatures as a function of frequency. Nayereh Soltani et.al.[24] Reported Zirconia nanoparticles using direct calcination of an aqueous solution containing zirconium acetate as metal precursor and polyvinylpyrrolidone as capping mediator. The subjected thermal treatment method exclusive of drying process was able to remove the organic compounds efficiently during the calcination process and leave behind the residue of crystalline ZrO2 nanoparticles. It was also revealed that the calcination temperature is a key factor in controlling the particle size from 7 to 32 nm when calcination temperature increased from 600 to 900∘C,respectively. The band gap energy of ZrO2 nanoparticles decreased from4.83 eVat 600∘Cto4.74 eVat 900∘C as a result of increasing particle size.This modified thermal treatment to synthesize ZrO2 nanoparticles is a very straight forward, cost effective, and environmentally friendly method, which could be exploited for large-scale industrial fabrication. Miguel H. Boratto et.al.[25] presented the analysis of ZrO2 thin films obtained by nonalkoxide sol-gel method at different annealing temperatures. The results reported the relation between annealing temperature and impurities found in sol-gel zirconia thin films as well as their relationship with the capacitive characteristic of the dielectric layer, which is a fundamental property for specific electronic applications and at specific frequency operations, such as in field effect transistors (FET). Zirconia thin films annealed at 450 °C have presented high transparency, homogeneous and non-porous surface, and optical band gap of 5.8 eV. The study of the thin film composition showed residues of S and Cl elements from the precursor solution that contribute for the reduced dielectric constant of the zirconia thin films through the increase of dipole and ionic relaxations, that deteriorates the dipole formation in the dielectric film. Even though a lower dielectric constant was found due to such impurities, it is still higher than SiO2 dielectric constant, which indicates a possibility of application of the ZrO2 deposited by sol-gel for replacement of the latter oxide in electronic devices. In addition, MIM devices on glass and polymeric substrates presented high electric resistivity and specific capacitance, even at annealing temperature as low as 100 °C. Both findings were indispensable characteristics for applications as insulating dielectric layer in electronics, and specifically in FETs. In summary, The reported showed that

lower annealing temperature contributes to higher impurity concentration within the ZrO2 film, which depreciates its dielectric characteristics. However, all the results shown in this communication suggest that zirconium oxide obtained through non-alkoxide sol-gel method presents competitive characteristics for application in capacitors and transistors. Soylu et.al.[26] studied Pure metal oxide catalysts were synthesized by co-precipitation and sol-gel method. The monoclinic nanorod structured Bi2O3 showed the highest percentage of 4-nitrophenol degradation (100%) and highest reaction rate (0.029 mg l_1 min_1). Finally, the structural and optical properties of Bi2O3 catalyst led to a profound positive effect on the photocatalytic activity for degradation of 4-nitrophenol. H.Asiabi et.al [27] reported the synthesis of a novel nano-adsorbent MWCNT/ZrO2and its application as coating for HF-SPME fiber. This nano adsorbent was developed for the extraction of six PAHs from environmental waters, coffee, and tea samples. The fiber was proved to have good mechanical and chemical stability, high extraction capacity, and high surface area. In addition, it is reusable. The synthesis of the adsorbent and HF-SPME procedure was also rapid and simple with high clean-up and selectivity, which made the method suitable for the analysis of PAH in complex matrices.This method, coupled to HPLC-UV analysis, exhibited a wide linear range, low detection limit, suitable repeatability, and high recover-ies of six PAHs. Marcin Banach et. al.[28] synthesized ZnO crystallites with different amounts of ZrO2 via a precipitation method with the help of microwave irradiation. Results showed that the addition of ZrO2 significantly increased the photocatalytic properties of ZnO. Different widths of energy bands occurring in both oxides contributed to reducing the distance between the conduction bands and the valence bands in the whole composite. An increase in the mass of the bed, an increase in the pH of the solution, and a decrease in the initial concentration of MB caused the photocatalytic efficiency of ZrO2–ZnO to be over 97% after just 30 min. The photocatalytic activity of cationic dye MB was greater than the photodegradation of anionic dye MO. Inamdar et.al.[29] have synthesized ZrO2 nanoparticles by chemical co-precipitation method using zirconium sulphate and sodium hydroxide as a starting materials. Effect of calcination temperature on structural and optical properties of ZrO2 nanoparticles were investigated. XRDspectra confirms the tetragonal phase at calcination temperature 600 °C and crystallinity of samples increases with increase in calcination temperature. At the calcination temperature 800 °Cthe phase transition from tetragonal to tetragonal-monoclinic mixed phase is noticed. The FESEM images show that the particles are of

irregular shape and of nanometer scale. Energy dispersive X-ray analysis (EDX) reveals the elemental composition of ZrO2 nanoparticles. The FTIR spectra confirms the formation of ZrO2. The optical band gap is calculated fromUV–vis absorption measurement. It was found that the strong quantization and varying band gap with calcination temperature. The fluorescence emission spectra shows change in emission wavelength and intensity with calcination temperature. At calcination temperature 800 °Cemission intensity is decreased which may be due to the phase change and the formation of surface defects such as oxygen vacancy and interstitials. Significant modification were observed in structural, photoluminescence and life time measurements due to calcination temperature and thus makes ZrO2 a promising material for optoelectronic applications. Mohammad Hayath Rajvee et.al. [30] have studied electrical characteristics of the high-k dielectric layer of Zirconium Titanate (ZrTiO2) prepared using Sol-Gel based spin coating technique. Initially, titanium doped zirconium dioxide solution is prepared using the Sol-Gel method; after preparation of the solution, it is tested for conductivity, which is 10-8 siemens/cm. This confirms the prepared material's suitability to be used as a dielectric material. The solution was then deposited on glass substrates and p-Si(100) using the spin coating method at varying speeds of 4000, 5000, and 6000 rpm. The films are characterized for their chemical, structural and ectrical properties. From the XRD graph, FESEM results known that the prepared films are purely amorphous. & the thin film is found to be smooth, and a uniform. From the EDX results, the Zr:Ti ratio is shown as 1:2. The thickness of the thin film is obtained by characterizing the film using a spectroscopic ellipsometer. Film thicknesses were 44, 41, and 40 nm respectively for 4000, 5000, and 6000 rpm spin rates. Thus it satisfies the relation, i.e., the spin speed is inversely proportional to the film thickness. Obtained Leakage currents are much lower than the reported gate leakage current density. The values obtained from Agilent 1500A Semiconductor Device Analyzer are 152 nA, 26.7 nA, and 369 nA, respectively, for different spin rates. Maximum accumulation capacitance (Cmax) values are 15.2 nF, 13.2 nF and 18.3 nF. Calculated dielectric constant (k) values from the accumulation capacitance are 37.6, 32.1, and 29.1, respectively, for three different spin rates.

Conclusion :

The last decades research shows that zirconia nanoparticles are easily obtained by various chemical methods. In the synthesis of zirconia by sol-gel method the size & morphology of

nanocrystalls dependent on precursor used.The hydrothermal method & chemical co-precipitation is a costsaving method to analyze & charactrise the comprehensive data ,ability to get improving quality of zirconia & metal carbides.Co-precipitation & precipitation methods also run via sol-gel method to get metal oxides & zirconia particles.. The study shows that the some amount of dopant ions affect the sensitivity of the sensor. The more sensitive ions enhances the sensitivity of the material.The Sol-gel mehods prepare ZrO2 particles shows photocatalytic properties in condensation & hydrolysis reactions.

ZrO2 nanoparticles are having multifunctional approach in reseach institutes & in industrial applications use. However more studies & better approach to enhance ecofriendly methods to adapt to synthesize the ZrO2 particles to save the environment pollution like to prevent toxic materials from nature & contaminated natural water .

References:

[1] Mamak M, CoombsNand OzinGA 2001 Chem. Mater 13 3564

[2] Zhang R, Zhang Xand HuS 2010 Sens. Actuators B 149 143

[3] Wang X, Zhai B, Yang M, HanWand Shao X2013 Mater. Lett. 112 90.

[4] Zhang X, SuHand Yang X2012 J. Mol. Catal. A: Chem. 360 16

[5] Gusmano G, Montesperelli G, Rapone M, Padeletti G, Cusma A, Kaciulis S and Mezzi A 2007 Surface&Coatings Tech. 201 5822

[6] Zhang C, Li C, Yang J, Cheng Z, Hou Z, Fan Y and Lin J 2009 Langmuir 25 7078

[7] IlkhechiNN, Kaleji BKand Salahi E 2014 Opt. Quant. Electron. 47 1187

[8] Carvalho JM, Rodrigues LCV, FelintoMCF, Nunes L A O, Hols J and BritoHF 2015 J. Mater. Sci. 50 873

[9] Chen Q, Chang Y, Shao C, Zhang J, Chen J, WangMand Long Y 2014 J. Mater. Sci. Technol. 30 1103

[10] Zhu H, YangDand Xi Z 2007 J. Am. Ceram. Soc. 90 1334

[11] Purohit RD, Saha S and TyagiAK2006 Mater. Sci. Eng. B 130 57

[12] Lan L, Chen S, Cao Y, Zhao M, GongMand Chen Y 2015 J. Colloid . Interface Sci. 450 404

[13] N C Horti, M D Kamatagi, S K Nataraj ,M N Wariand, S R Inamdar Nano Express 1 (2020) 010022.

[14] V. Santos, M. Zeni, C.P. Bergmann and J.M. Hohemberger, Adv.Mater.Sci. 17(2008) 62-70

[15] Masoud Salavati-Niasari, Mahnaz Dadkhah b, Fatemeh Davar a Inorganica Chimica Acta 362 (2009) 3969–3974

[16] H.S. Chen, R.V. Kumar, B.A. Glowacki, Materials Chemistry and Physics 122 (2010) 305–310

[17] Sadok Letaief, Yun Liu, and Christian Detellier Can. J. Chem. 89: 280–288 (2011) doi:10.1139/V10-142

[18] Mohammed Rafiq Hussain Siddiquia*, Abdulaziz Ibrahim Al-Wassila,Abdullah Mohmmed Al-Otaibib, Refaat Mohamad Mahfouza Materials Research. 2012; 15(6): 986-989

[19] Hang Cui , Qi Li , Shian Gao , Jian Ku Shang Journal of Industrial and Engineering Chemistry 18 (2012) 1418–1427

[20] N. Clament Sagaya Selvam a, A. Manikandan a, L. John Kennedy b, J. Judith Vijaya a, Journal of Colloid and Interface Science 389 (2013) 91–98

[21] R. Madhusudhana1, M.A. Sangamesha2, R. Gopal Krishne Urs3, L. Krishnamurthy4, G.L. Shekar5 ISSN 2320-5407, International Journal of Advanced Research (2014), Volume 2, Issue 4, 433-436

[22] Wei Jiang, Jian He, Jiemin Zhong, Jiuyun Lu, Shaojun Yuan, Bin Liang, Applied Surface Science, Volume 307, 15 July 2014, Pages 407-413.

[23] Suresh Sagadevan, Jiban Podder and Isha Das, J Mater Sci: Mater Electron

DOI 10.1007/s10854-016-4469-6

[24]Aysar S. Keiteb, Elias Saion, Azmi Zakaria, and Nayereh Soltani , Journal of Nanomaterials, Volume 2016, Article ID 1913609, 6 pages.

[25] Miguel H. Boratto, Mirko Congiu, Stevan B.O. dos Santos, Luis V.A. Scalvi ,Ceramics International 44 (2018) 10790–10796

[26] Wusiman Muersha, Gulin Selda Pozan Soylu, Journal of Molecular Structure xxx (2018) 1-7

[27] Mahnaz Nozohour Yazdi, Yadollah Yamini∗, Hamid Asiabi Journal of Chromatography A, 1554 (2018) 8–15

[28] Olga Długosz, Krzysztof Szostak ,Marcin Banach Applied Nanoscience

https://doi.org/10.1007/s13204-019-01158-3

[29] NCHorti, MDKamatagi, SKNataraj, MNWari and SR Inamdar Nano Express 1 (2020) 010022

[30] Mohammad Hayath Rajvee , S.V. Jagadeesh Chandra , P. Rajesh Kumar, CH.V.V. Ramana , Kalahasthi Neelama , R. S. Dubey biointerfaceresearch Volume 11, Issue 5, 2021, 12761 – 12768

Paper-34

RGB color space based Machine Vision system for classification of Guava fruits

Sharad Bangayya , Shrikant Gandhe, Ashok Kanade

Department of Electronic Science, P.V.P. College, Pravaranagar, India,

ABSTRACT

Abstract: *In the present work, a general approach is developed to estimate the ripeness level of Guava fruit without touching it. This work deals with the study of using an artificial computer based vision system as a non-destructive instrument to analyze fruit ripeness stage. The cultivar chosen for this study is Guava fruit. This paper presents a simple method that uses a combination of digital web camera, computer, and self developed graphics software to measure and analyze the surface color of fruits. The method has also the advantages of being versatile and affordable. The images of the fruits can be displayed on computer screen or printed on paper for qualitative analysis of color and structure. Quantitative information such as RGB color distribution, Chromaticity coordinates according to CIE1931 standard and averages (in terms of L_, a_ and b_ values) can also be determined readily.*

Keywords: RGB Color, fruit ripeness,computer vision, guava fruit classification

1. Introduction

Sorting of fruits on the basis of their ripening stage has been an issue faced by producers as well as sellers due to the sheer volumes handled and the delicate nature of the fruit. In the case of agricultural products, good efforts andappropriate techniques are necessary to distinguish between various ripening stages of fruits when using machine vision for sorting [1].

The increased awareness and sophistication of consumers have created the expectation for improved quality in consumer food products. This in turn has increased the need for enhanced quality monitoring. Quality itself is defined as the sum of all those attributes which can lead to the production of products acceptable to the consumer when they are combined. Quality has been the subject of a large number of studies. The basis of quality assessment is often subjective with attributes such as appearance, smell, texture, and flavour, frequently examined by human inspectors. Consequently Francis (1980) found that human perception could be easily fooled. Together withthe high labour costs, inconsistency and variability associated with human inspection generate the need for objective measurements

systems. Recently automatic inspection systems, mainly based on camera–computer technology have been investigated for the sensory analysis of agricultural and food products. This system known as computer vision has proven to be successful for objective measurement of various agricultural and food products. Computer vision includes the capturing, processingand analysing images, facilitating the objective and non destructive assessment of visual quality characteristics in food products. The potential ofcomputer vision in the food industry has long been recognized and the food industry is nowranked among the top 10 industries using this technology [2]. Recent advances in hardwareand software have aided in this expansion by providing low cost powerful solutions, leading to more studies on the development of computer vision systems in the food industry. As a result automated visual inspection is under going substantial growth in the food industry because of its cost effectiveness, consistency, and superior speed andaccuracy. Traditional visual quality inspection performedby human inspectors have the potential to be replaced by computer vision systems for many tasks [1-4]. There is increasing evidence that machine vision is being adopted at commercial level. This paper presents the latest developments and recent advances of computer vision in the food industry. Thefundamental elements of the systems and technologies involved are also examined.

Color and texture are the fundamental characterof natural images, and plays an important role in visualperception. Color has been a great help in identifyingobjects for many years.The process of color classification involvesextraction of useful information concerning the spectralproperties of object surfaces and discovering the bestmatch from a set of known descriptions or class models to implement the recognition task [2]. Texture is one ofthe most active topics in machine intelligence andpattern analysis since the 1950s which tries to discriminate different patterns of images by extractingthe dependency of intensity between pixels and theirneighboring pixels [1-4] or by obtaining the variance ofintensity across pixels [2-3]. Recently, different features ofcolor and texture are combined together for theirapplications in the food industry [5].Color features have been extensively appliedfor guava fruit quality evaluation mostly for defect detection and grading. For instance, color features of each pixel in imagesobtained in three components of RGB spaces could besuccessfully used for grading of guava fruits on the basis of their ripening stage.

This paper describes the development of a low cost machine vision system using webcams and image processing algorithms for classification and sorting of guava fruit. In this study, the main objective is to develop low cost machine vision system with appropriate algorithms to sort guava fruits with specific category of their ripeness as green, ripe, overripe

and spoiled. The system was to be used for automated sorting and it is integrated with image acquisition, image processing, and decision making algorithm.

2. System development

The system used low-cost webcams that required no frame grabber hardware, thus making the overall system cheaper and flexible from the design point of view. The images are taken by low cost webcam made by Iball [model i-C12.0].The Color images acquired in computer by self-developed image acquisition software programmed using LabVIEW2012 with Vision development suit. The RGB values are evaluated from images using express VI available in LabVIEW. From this RGB values the CIE1931 chromaticity coordinates are calculated and also tristimulus values are evaluated from it. The fuzzy logic based sorting algorithm is used. The decision making is achieved for showing the class of fruit on the computer screen as green, ripe, overripe and spoiled.

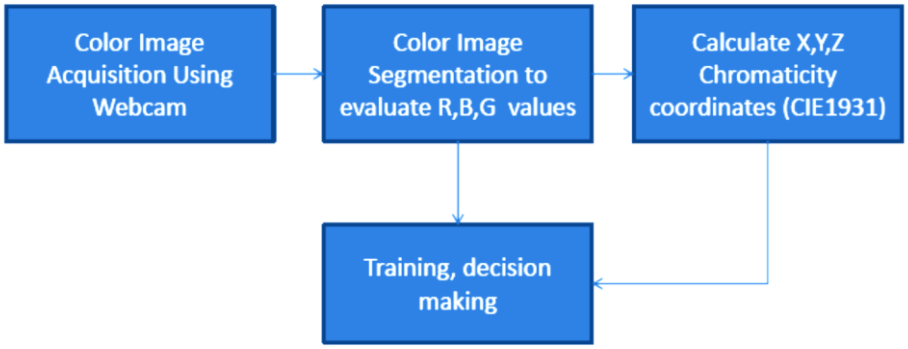

Figure 1 Block Diagram of system

Figure 2 Developed System

3. Image acquisition and illumination hardware

The iball made 12 mega pixel web camera is used for image acquisition. This camera has six white LED for illumination. The LED brightness is controllable through

potentiometer is provided on interface cable. The LUX meter is used for this purpose. This LED used having color temperature near to white light. The spectral characteristics of illuminating source are characterized using sterllar Net miniature spectrometer systems and software. The spectral characteristics are shown in figure 3.

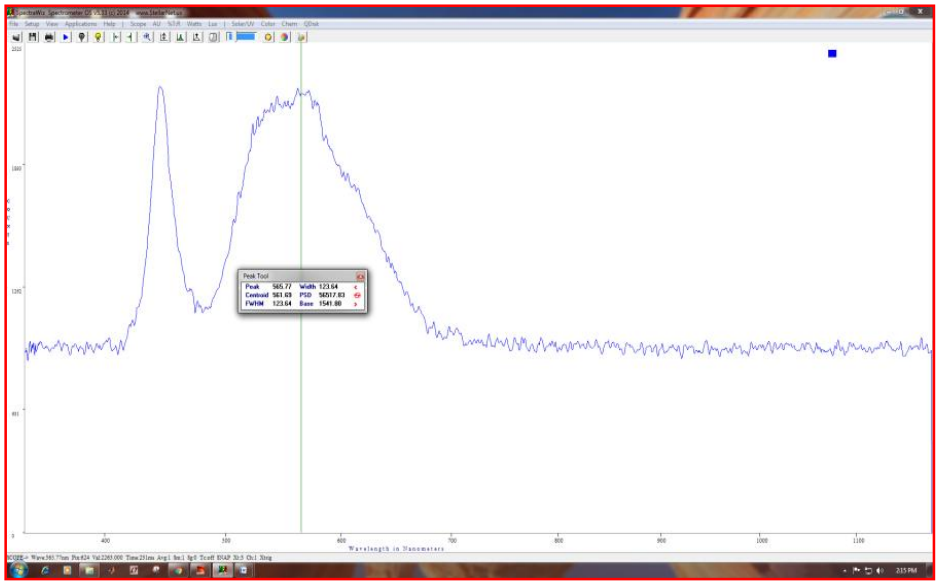

Figure 3 Spectral characteristics of illumination source

This plot indicates two peaks, lower peak has peak wavelength of 445.88 nm and upper peak has peak wavelength of 565.77 nm. The CCT in the range of 5000 ^{o}K to 8000^{o}K.This illumination system provides a uniform light intensity over the fruit sample plane as shown in figure 3.40.

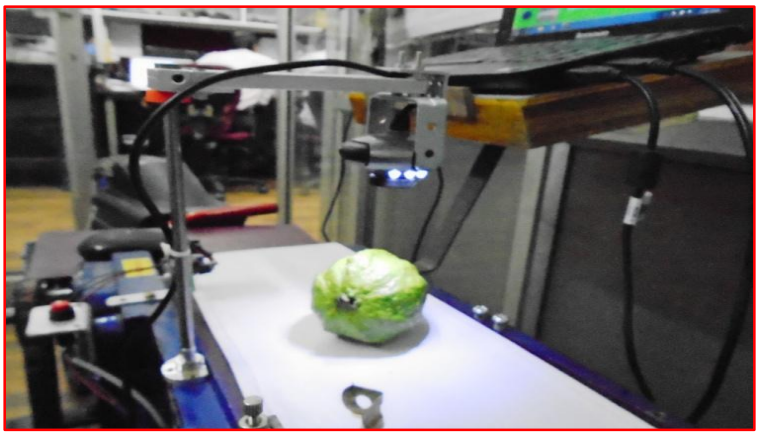

Figure 4 Fruit under webcam with integrated light illumination source

A digital web camera iball i12 was located vertically at a distance of 10 cm from the sample. The angle between the camera lens axis and the lighting sources was around 45^{0}. The experimentation with this illumination system is performed inside a close room whose internal walls were painted with dark color to avoid the light reflection.

4 Fuzzy logic based pattern recognition VI

In the present application, model for classification of guava fruits is developed using the fuzzy logic and mean RGB color values of fruit surface. The complete software module is developed image acquisition, pre-processing and fuzzy based pattern recognition. The image acquisition, illumination method, image segmentation is already explained in above sections of this chapter. The two modules were developed for prepackaging and storage shelf-life based classification of guava fruits.

The mean RGB values of each class of fruit were used to train the classifier. The fuzzy logic module is designed and implemented in LabVIEW using fuzzy system designer. Figure 5 shows the front panel user interface of developed software for guava fruit classification using fuzzy logic.

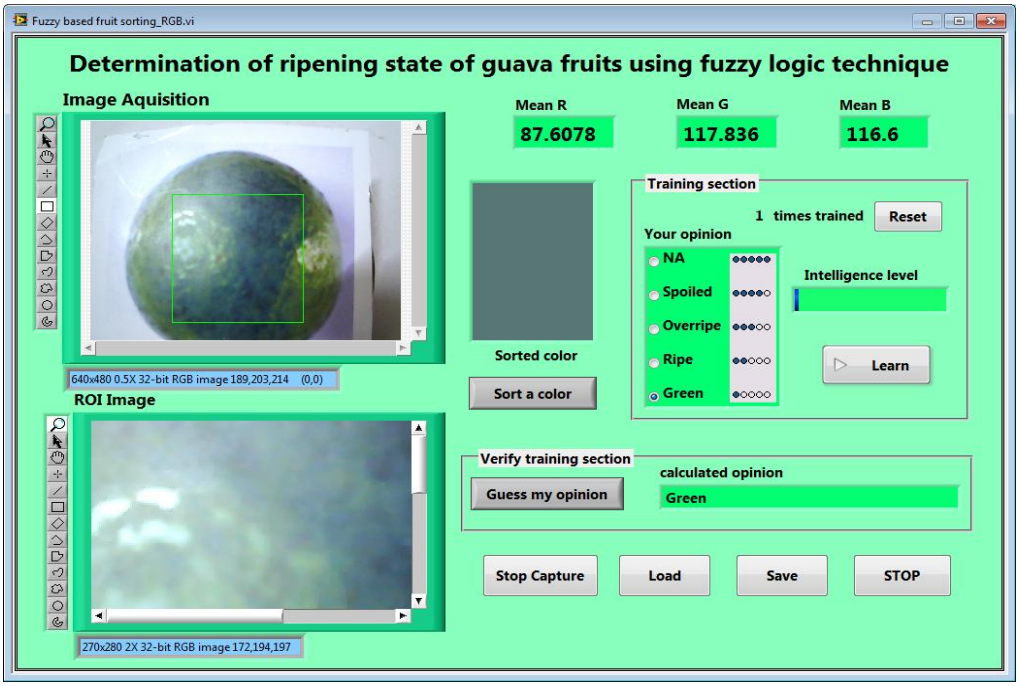

Figure 5. User interface of fuzzy logic based classifier VI

The developed system starts the process by capturing the fruit's image using an iball webcam. The feature extraction process is achieved using the image processing express VIs available in LabVIEW12 with vision development suit. The ROI image was extracted from acquired image. The mean RGB values from ROI of image is evaluated using Image Color Histogram VI .This includes the mean of each color plane. Figure 6 Shows block diagram of sorting Process.

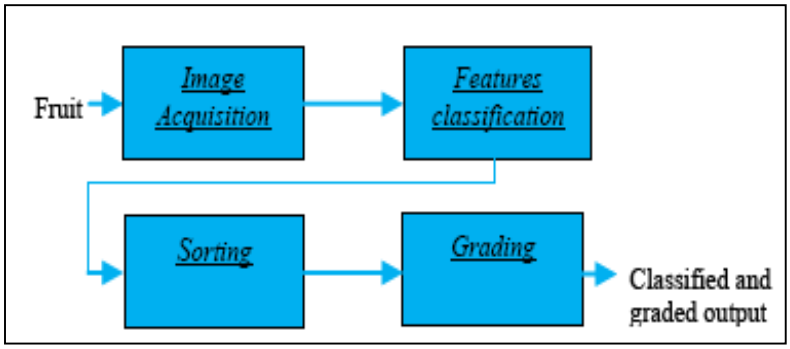

Figure 6. Block diagram of sorting and grading process

The fuzzy logic module consists of following processes.

1. FIS Editor 2. Membership Function Editor 3. Rule Editor 4. Rule Viewer 5. Surface Viewer

The process starts with deciding the system inputs and outputs followed by the definition of input and output membership functions. Finally, the rules are constructed using IF-THEN statements using rule editor. The system works according to the rules set by the expert. Hence this is a critical step in the grading process. The rule and surface viewer are the graphics that are used to view the built system.

5. Experimentation with developed system

The developed machine vision based fruit sorter system is used for pre-packaging classification of guava fruits into four classes. 100 fruits samples of each ripening class were used for experimentation. The 50% of the fruit images from each group were used to train the PARC module and the remaining 50% fruits used for testing. The images of training set samples were captured at various times of the day for the each class. This method increase the data set variability and represent a more realistic scenario. The RGB color space and CIE 1931 chromaticity coordinates are used. The classification accuracy obtained using developed system for the four classes of guava fruit is presented in Table1

Table 1 Experimental Observations

Ripening state	No. of samples		Classification		performance %
	Training	Testing	Expert	System	
Green	50	50	50	50	100
Ripe	50	50	50	40	80
Overripe	50	50	50	44	88
Spoiled	50	50	50	46	92

6. Result and Conclusion

The average efficiency achieved using developed classifier system is about 90%, if human grading taken as reference level is assumed to be 100% accurate. However, 10% variation is also due to individual judgment of human-graders in perceiving the ripening level of fruit during manual grading, which of course is inevitable. The repeatability of the developed system is found to be 100% from rigorous experimental work.

References:

[1] B. Ojeda-Magana, R. Ruelas, J. Quintanilla-Domingvez and D.Andina, "Colour Image Segmentation by Partitional ClusteringAlgorithms", IECON 2010 - 36th Annual Conference on IEEEIndustrial Electronics Society, 7-10 Nov., Glendale, AZ, 2010,pp.2828 -2833.

[2] Meenu Dadwal, V.K. Banga, "Estimate Ripeness Level of fruits Using RGBColor Space and Fuzzy Logic Technique"International Journal of Engineering and Advanced Technology (IJEAT),ISSN: 2249 – 8958, Volume-2, Issue-1, October 2012,page225.

[3] S.Arivazhagan1, R. Newlin Shebiah1, S. Selva Nidhyanandhan1, L.Ganesan2"Fruit Recognition using Color and Texture Features"Journal of Emerging Trends in Computing and Information Sciences,VOL. 1, NO. 2, Oct 2010, E-ISSN 2218-6301, page 90.

[4] Kit L. Yam , Spyridon, E. Papadakis, "A simple digital imaging method for measuring and analyzing color of food surfaces"Journal of Food Engineering 61 (2004) 137–142

[5] Tadhg Brosnan, Da-Wen Sun "Improving quality inspection of food products by computer vision—a review"Journal of Food Engineering 61 (2004) 3–16

[6] Domingo Mery, Franco Pedreschi "Segmentation of colour food images using a robust algorithm, Journal of Food Engineering 66 (2005) 353–360.

[7] T. Rivas, J.M. Matías, J. Taboada, C. Ordonez "Functional experiment design for the analysis of colour changes in granite using new L* a* b* functional color coordinates" Journal of Computational and Applied Mathematics 235 (2011) 4701–4716

Paper-35

Dielectric relaxation studies of potentised homeopathic medicine in the frequency range of 20 Hz to 2 MHz

G. R. Mahajan [1], Y.S. Joshi [2], K. S. Kanse[3], A.C. Kumbharkhane[4*]

[1]Department of Physics, Shri Datta Arts, Commerce and Science College Hadgaon Dist: Nanded, Maharashtra, India.
[2]Department of Electronics, Lal Bahadur Shastri Mahavidyalaya, Dharmabad Dist: Nanded, Maharashtra, India.
[3]Department of Physics, Lal Bahadur Shastri Mahavidyalaya, Dharmabad Dist. Nanded, Maharashtra, India.
[4]School of Physical Sciences, S. R. T. M. University, Nanded, Maharashtra, India.

ABSTRACT

The complex relative dielectric properties of homeopathic medicine Cuprum Metallicum with different potencies have been measured using precision LCR meter in the frequency range of 20 Hz to 2 MHz at 25ºC. The electrical and dielectric properties of the Cuprum Metallicum are represented in terms of complex dielectric function ε*(ω), electrical modulus M*(ω), electrical conductivity σ*(ω). All theses parameters are used to explain the various processes associated with the electric and dielectric properties of Cuprum Metallicum.

Keywords: Precision LCR meter; complex permittivity; electric modulus.

1. Introduction:

Homeopathy originated as a new medical approach in early 18th century is based on definite scientific and artistic concepts. The system is based on seven principles/ theories, codified by Dr Hahnemann, its founder. The practice of homeopathy was well accepted by the public from the very inception due to safety of medicine and effectiveness. The popularity of homeopathy spread across the globe even during the life time of its founder. It was considered as one of the refined medical systems till about 1950s. Homeopathy is a distinctive medical specialty being practiced across the world. The system has blended well into the roots and traditions of many countries and plays an important role in providing health care to a large number of people [1, 2].

Homeopathy is controversial because medicines in high potencies such as 30C and 200C involve huge dilution factors (10^{60} and 10^{400} respectively) which are many orders of

magnitude greater than Avogadro's number, so that theoretically there should be no measurable remnants of the starting materials. No hypothesis which predicts the retention of properties of starting materials has been proposed nor has any physical entity been shown to exist in these high potency medicines [3].

Homoeopathic potentisation of Hahnemannian era constituted of serial dilution followed by either trituration or succession or both depending on the type of drug substances. In the preparation of potencies from solid drug substances, decimal and centesimal scales are used. In the preparation of liquid drug substances, manufacturing of homoeopathic medicines is from the mother solution (tincture) by serial dilution and succussion (mechanical agitations) in one of the three potency ranges, decimal (1:9), centesimal (1:99), or fifty‑millesimal. Solid insoluble materials (e.g.*Cuprum metallicum*) are triturated with lactose in the ratio of 1:10 till the 6X potency, after which the liquid dilutions are carried out [4]. The liquid dilutions are prepared by the Hahnemannian method [5] till the 200C potency and the Korsakovian method for potencies beyond 200C.

Cuprum metallicum, derived from pure metallic copper, is a medication frequently used in homeopathy. The dielectric dispersion occurring in potentised homeopathic medicines subjected to variable frequency electric field was studied by using an instrumentation method developed by C R Mahata [6]. The experimental results for three potencies of Cuprum Metallicum (Cuprum met) in the frequency range of 100 kHz - 1 MHz was reported [6]. Using dynamic light scattering (DLS) and high-resolution transmission electron microscopy (HRTEM) studies, Ghosh *et al*.[7] have reported that the size of *Cuprum metallicum* drug particles indeed decreases with increase in potency. Dielectric dispersion studies were conducted in a broad range in a frequency range of 100 KHz to 50 MHz with potencies below and above the Avogadro limit by taking 6C and 30C potencies of *Graphite's* and *Cuprum Metallicum* in liquid form. Measurements were made with an Anomalous Dielectric Dispersion Detector (A3D) [8]. The theory and instrumentation techniques related to potentised homoeopathic medicines are discussed in detailed, T. Maity *et al* [9]. Also in Midmore *et al* [10] measurements are carried out on the basis of the effect of particle volume fraction on the dielectric response of concentrated lattices in the frequency range1Hz–10MHz, a range where the theory predicts large dielectric dispersion effects. Anomalous dielectric dispersion in ordered molecular groups also studied. Some paper simplifies the identification of potentised homoeo-medicines through spectral signature obtained by dielectric dispersion effect [11]. That homoeo-medicines cannot be anything except specifically ordered molecular groups, is theoretically proposed by Mahata [12-15]. There are many theoretical and

experimental explanations advanced by different researchers since last 50 years from different areas of science which is briefly reported in a review literature [16].

Dielectric behaviors of different non–homeopathic and non–medicinal substances both in solid and liquid forms are reported in different research works. There are research publications dealing with dielectric dispersion effects in the different types of organic and inorganic materials but not for potentised homeopathic medicines.

In the present study, the complex relative permittivity spectra of homeopathic medicine *Cuprum Metallicum* with different potencies (6C, 12C, 30C, 200C, 1M, 10M) have been measured using precision LCR meter in the frequency range of 20 Hz to 2 MHz at 25ºC. The electrical and dielectric properties of the *Cuprum Metallicum* are represented in terms of complex dielectric function ε*(ω), electrical modulus M*(ω), electrical conductivity σ*(ω).

2. Experimental

2.1 Materials

Homeopathic medicines *Cuprum Metallicum* with different potencies (6C, 12C, 30C, 200C, 1M, 10M) used for experimental purpose are taken from an *SBL PVT LTD.* well-known international company for world class homeopathic medicines.

2.2 Measurement

The complex relative dielectric function ε*(ω) of *Cuprum Metallicum* were determined by using Agilent E4980A precision LCR meter. A four terminal dielectric test fixture, Agilent 16452A was used for capacitance and resistance measurement in the frequency range 20Hz to 2MHz. The capacitance and parallel resistance of the liquid dielectric test fixture without and with samples were measured to compensate for a short [17]. The test fixture correction coefficient was also considered to cancel the effect of stray capacitance during the evaluation of the value of the complex dielectric function. The complex dielectric function ε*(ω) of the materials is determined using Eq.1.

$$\varepsilon^*(\omega) = \varepsilon'(\omega) - j\varepsilon''(\omega) = \alpha\left[\frac{C_P}{C_0} - j\frac{1}{\omega C_0 R_P}\right] \qquad (1)$$

Where ω=2πf is the angular frequency and α is the correction coefficient of the cell. All measurements were made at 25ºC.

3. Results and Discussion:

3.1 Complex relative permittivity:

Fig. 1 shows the frequency dependent spectra of the real part of the relative dielectric

function ε' for *Cuprum Metallicum* at different potencies. It is observed that the dielectric permittivity for *Cuprum Metallicum* have very high value at lower frequency and these values lowers up to 10^3 Hz frequency then constant over the range.

Fig. 2 shows the frequency dependent spectra of dielectric loss, tanδ for *Cuprum Metallicum* at different potencies. The tan δ spectra has the loss peak value corresponding to the electrode polarization relaxation frequency f_{EP}, which is used to calculate the electrode polarization relaxation time, $\tau_{EP} = (2\pi f_{EP})^{-1}$ [18, 19]. It (f_{EP}) is the frequency at which the bulk material property is separated out from the EP phenomena. From Fig.2 it can be seen that this frequency is highly sensitive to this potency. The τ_{EP} involves charging and discharging time of EDL capacitance, which is related with the dynamics of the absorbed ions on the electrode surfaces in the alternating electric field. The electrode polarization relaxation times for *Cuprum Metallicum* at different potencies are plotted in Fig. 3. The variation of τ_{EP} as a function of potencies is shown in Fig.3. Figure shows the lowest peak at 1M potency of *Cuprum Metallicum* correspondingly Fig.5 shows a highest value of dielectric constant.

3.2 Electrical modulus:

The frequency dependent values of M*(ω) is obtained using Eq.2 [20, 21].

$$M^*(\omega) = \frac{1}{\varepsilon^*(\omega)} = M' + jM'' = \frac{\varepsilon'}{\varepsilon'^2 + \varepsilon''^2} + j\frac{\varepsilon''}{\varepsilon'^2 + \varepsilon''^2} \qquad (2)$$

The main advantage of this formulation is that, the space charge effects often do not mask the features of the spectra, due to suppression of high capacitance phenomena in M"(ω) plots. Fig. 4 shows the complex electric modulus for *Cuprum Metallicum* of different potencies at room temperature. The real part of modulus M'(ω) values is very low in the lower frequency region. It increases for higher frequency in between 100 KHz to 1MHz and attains steady after that. The imaginary part of modulus M"(ω) spectra shows a higher value for low potencies and decreases with increase in potencies. Fig.4 (b) exhibits M" peak value, the frequency fσ corresponding to these peaks is associated to the most probable ionic conductivity relaxation time $\tau_\sigma = (2\pi f\sigma)^{-1}$ [19]. From the graph of M"(ω), ionic conductivity relaxation time (τ_σ) corresponding to the peak values of M"(ω) are determined and tabulated in Table 1.

3.3 Complex conductivity:

The frequency dependent real part σ' and the imaginary part of σ" of the alternating current

(ac) complex conductivity σ*(ω) of the liquid samples were obtained from the following Eq.3

$$\sigma^*(\omega) = \sigma' + j\,\sigma'' = \omega\varepsilon_0\varepsilon'' + j\varepsilon_0\varepsilon' \qquad (3)$$

where ε_0 is free space dielectric constant. Fig 6 shows the σ'(ω) spectra for *Cuprum Metallicum* at different potencies. From the σ'(ω) spectra for lower frequency it shows low values of conductivity and then after it almost constant over the frequency range.

3.4 Complex Impedance:

The complex impedance plane plots (Z'' vs. Z') are commonly used to separate the bulk material and the electrode surface phenomena. The frequency dependent values of the real part z' and reactive part of z'' of the complex impedance Z*(ω) of the liquids can be evaluated as:

$$Z^*(\omega) = Z' - jZ'' = \left[\frac{R_P}{1+(\omega C_P R_P)^2} - j\,\frac{\omega C_P R_P^{\,2}}{1+(\omega C_P R_P)}\right] \qquad (4)$$

Fig. 7 shows Z'' vs. Z' plots of *Cuprum Metallicum* of different potencies. This plot consists of semicircular arc in the high frequency region followed by a tail in the low frequency region telling a trend to another semicircular arc.

Conclusions:

The dielectric and electrical properties of *Cuprum Metallicum* of different potencies at 25°C has been well studied between the frequency ranges of 2Hz to 2MHz. Determined parameters such as complex dielectric function ε*(ω), electrical modulus M*(ω), electrical conductivity σ*(ω) and complex impedance Z*(ω) has been used to explain the electric and dielectric properties of the *Cuprum Metallicum* at different potencies. The highest value of dielectric constant at 1M potency of *Cuprum Metallicum* correspondingly shows lowest peak of electrode polarization relaxation times. The plot of A.C. conductivity confirms the effect of dipolar polarization.

Acknowledgements:

Financial support provided by Swami Ramanand Teerth Marathwada University, Nanded, Maharashtra [APDS/Uni.MRP/Sci.&Tech.-/Physics./2019-20/2835] is gratefully acknowledged. Also a financial support provided by SERB, DST, New Delhi

(SR/FTP/PS-203/2012) is thankfully acknowledged. Author GRM also thankful to Dr. D. N. Rander from Department of Physics, Lal Bahadur Shastri Mahavidyalaya, Dharmabad-431809 (M.S.), India, for helpful discussion.

References:

1. Eswara Das, Understanding the Principles of Homeopathy on A Research Perspective, J. Complement Med Alt Healthcare, J 9(2): JCMAH.MS.ID.555756 (2019).
2. R. P. Upadhyay, C. Nayak, Homeopathy emerging as nanomedicine, Int. J. High Dilution Res. 10(37) (2011) 299-310.
3. P. S. Chikramane1, A. K. Suresh, J. R. Bellare, S. G. Kane1, Extreme homeopathic dilutions retain starting materials: A nanoparticulate perspective, Homeopathy 99 (2010), 231-242.
4. A. L. Gayen, D. Mondal, D. Bera, P. Biswas, B. K. Paul, D. S. Bhar, S. Das1, R. Narula, A. K. Khurana, R. K. Manchanda, P. Nandy, Effect of Cuprum metallicum potentised through both serial dilution and succussion in comparison to succussion alone on Escherichia coli bacterial system and electrical properties of poly (vinylidene fluoride‐co‐hexafluoropropylene) polymer, Indian Journal of Research in Homoeopathy, 13 (4) (October-December 2019).
5. Boericke and Tafel, Philadelphia, Hahnemann S. Organon of Medicine, 1901.
6. T Maity1, D Ghosh and C R Mahata, Effect of dielectric dispersion on potentised homeopathic medicines, Homeopathy 99 (2010), 99–103.
7. S Ghosh, M Chakraborty, S Das, R Basu, P Nandy, Effect of different potencies of nanomedicine *Cuprum metallicum* on membrane fluidity – A biophysical study, Am. J. Homeopath Med. 107(2014),161‐169.
8. C R Mahata, Dielectric dispersion studies of some potentised homeopathic medicines reveal structured vehicle, Homeopathy 102 (2013), 262-267.
9. T Maity, D Ghosh & C R Mahata, Theory and Instrumentation Related to Potentised Homoeopathic Medicines, Indian Journal of Research in Homoeopathy 2 (3), (July-September 2008), 1-5.
10. B R Midmore, R J Hunter and R W O'Brien. 'The Dielectric Response of Concentrated Lattices', Journal of Colloid and Interface Science, 120(1),(1987), 210 – 217.
11. T. Maity, D. Ghosh and C. R. Mahata, Theory and Instrumentation Related to Anomalous Dielectric Dispersion in Ordered Molecular Groups, Sensors & Transducers Journal, 85, 11, (November 2007), 1745-1756.

12. Mahata C. R., Homoeopathy explained in the light of recognized science. The homoeopathic heritage, Vol. 22, May 1997, pp. 245-252.
13. Mahata C. R., Some studies on physical basis of homoeopathic medicines, Journal of Technology, Vol. 29, 1, 1983, pp. 27–34.
14. Mahata C. R., Science and philosophy of medicines, National Institute of Homoeopathy Journal, Vol. S1, 1, Jan 1993, pp. 1-110.
15. Mahata C. R., Kent's Simple substances in the light of modern understanding of homoeopathic potency, Indian Journal of Classical Homoeopathy, Jan- March, 2002, pp. 42-45.
16. Benneth J. R., Seven Kinds of Proving for Homoeopathy.
17. Chaube H. A. & Rana, V. A. Solid State Phenomena (2014). 209, 182-185.
18. Sengwa, R. J. & Sankhla, S. Colloid and Polymer Science (2007). 285, 1237-1246.
19. Zhang, S., Dou, S., Colby, R. H. & Runt, J. J Non-cryst Solids (2005). 351, 2825-2830.
20. Pradhan, D. K., Choudhary, R. N. P. & Samantaray, B. K. Express Polymers Letters (2008). 2, 630-638.
21. Chanmal, C. V. & Jog, J. P. Express Polymer letters (2008). 2(4), 294-301.

Table 1: Static Permittivity (ε_0) & Ionic conductivity relaxation time (τ_σ) of *Cuprum Metallicum* of different potencies

Potencies of *Cuprum Metallicum*	Static Permittivity (ε_0)	Ionic Permittivity (τ_σ) (μs)
6C	29.68	1.0023
12C	29.69	75.1641
30C	30.22	79.6178
200C	30.05	63.2427
1M	30.33	56.3651
10M	29.70	89.3327

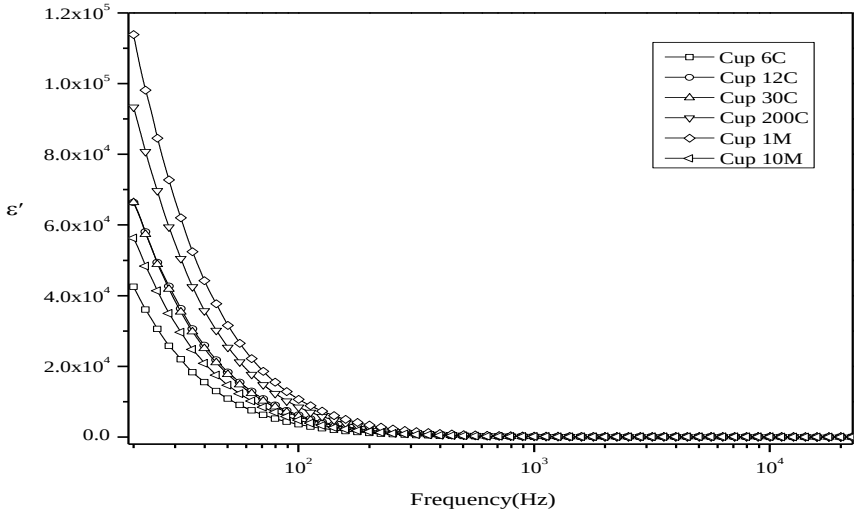

Fig.1 Shows the frequency dependent spectra of the real part of the relative dielectric function ε' for *Cuprum Metallicum* of different potencies.

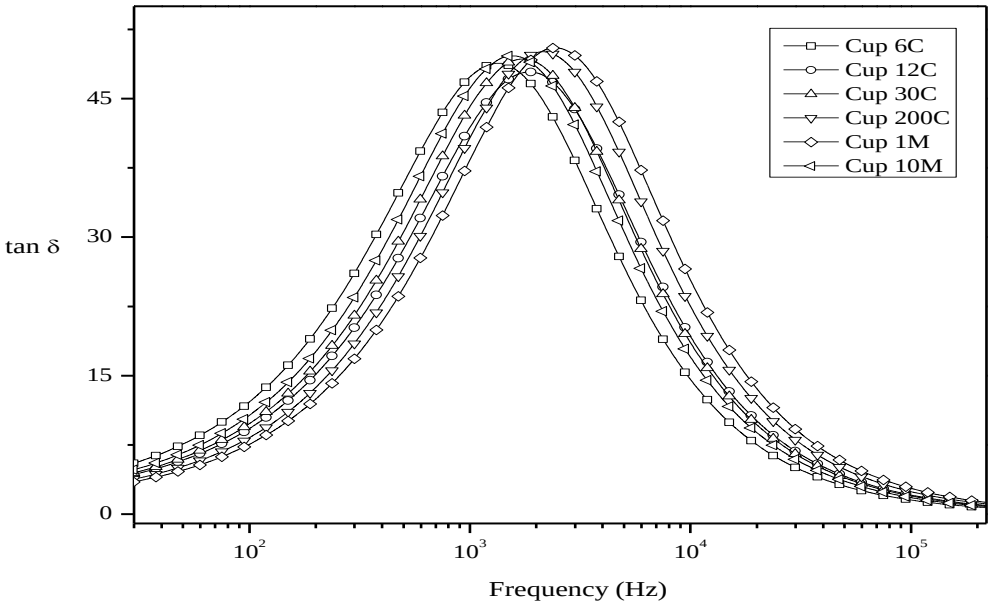

Fig.2 Shows the frequency dependent spectra of dielectric loss tangent,

tanδ for *Cuprum Metallicum* of different potencies.

Fig.3 The electrode polarization relaxation times vs. *Cuprum Metallicum* of different potencies.

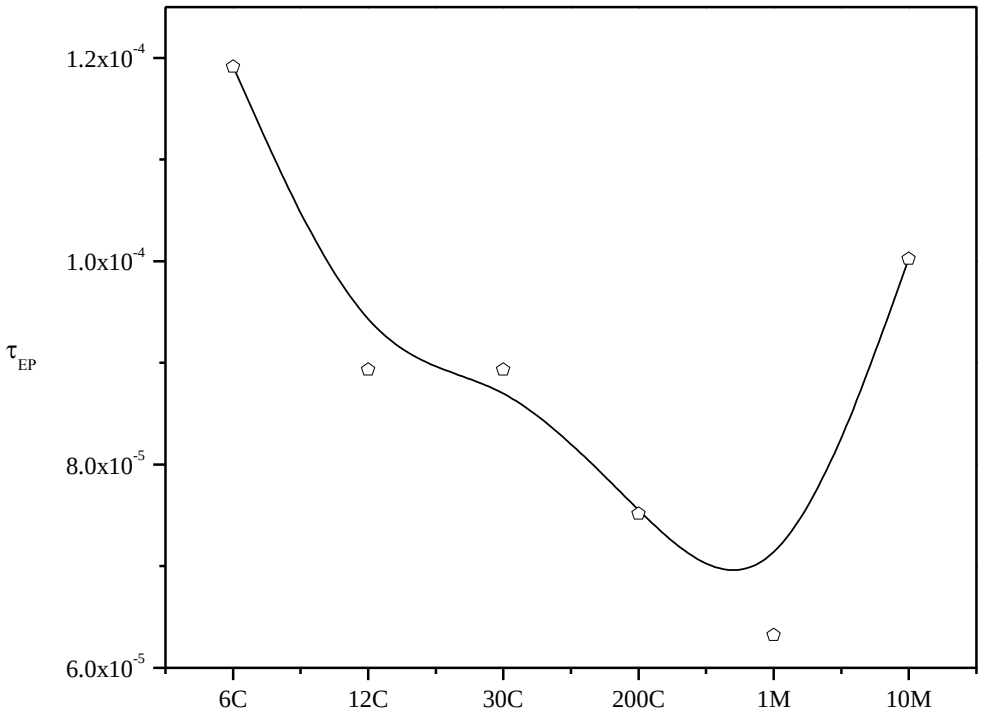

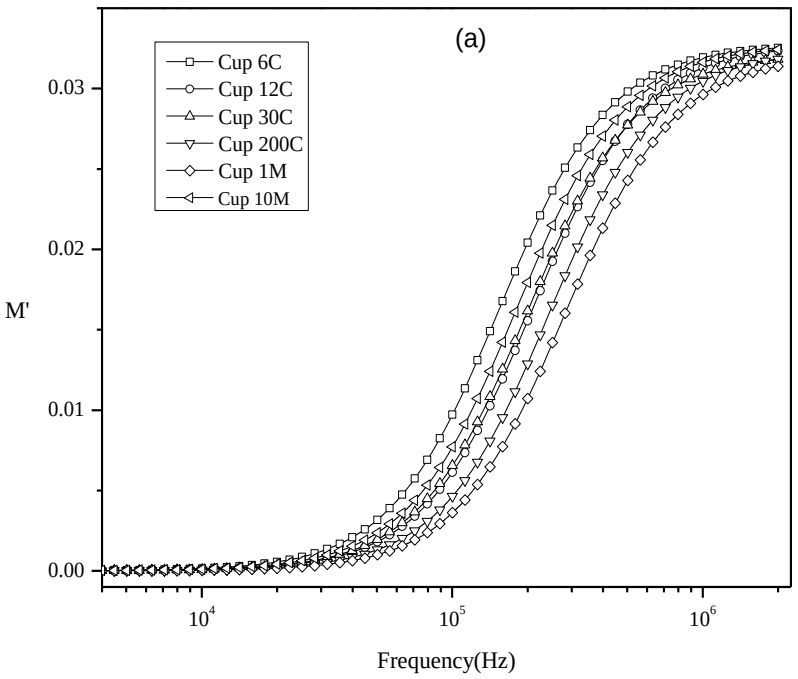

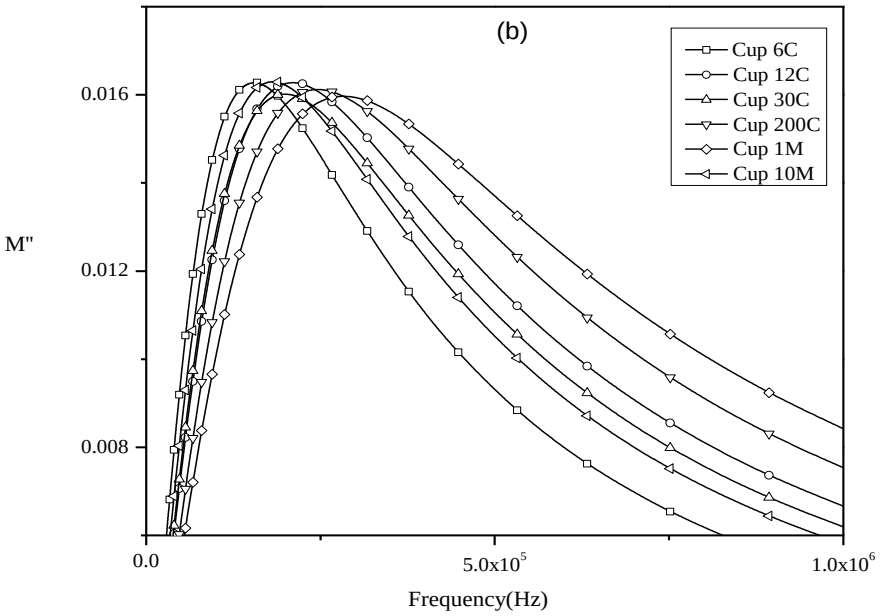

Fig.4 shows frequency and potencies dependent (a) Real part (M') and (b) Imaginary part (M") of the complex electric modulus [M*(ω)] for *Cuprum Metallicum*.

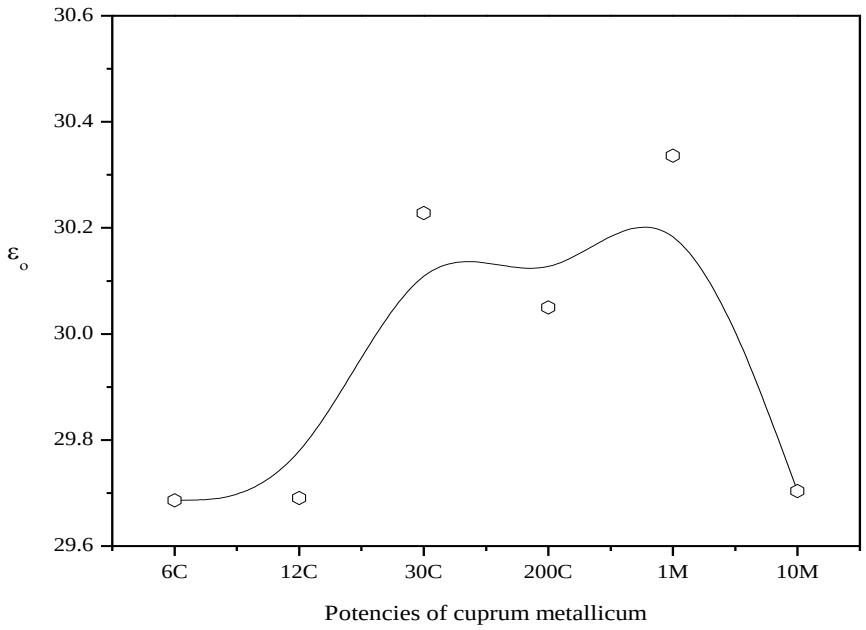

Fig.5 Static dielectric permittivity vs. different potencies of *Cuprum Metallicum.*

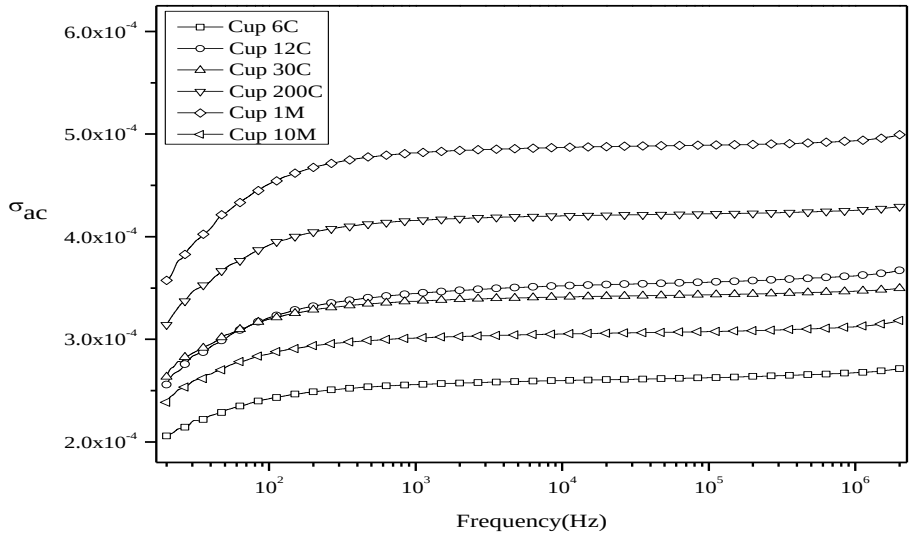

Fig.6 The σ'(ω) spectra for *Cuprum Metallicum* of different potencies.

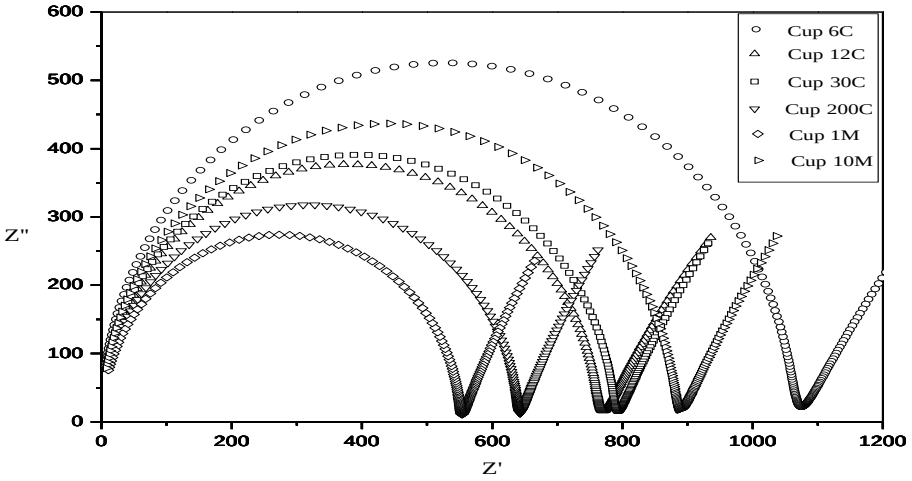

Fig.7 Complex impedance plot Z' vs. Z" for *Cuprum Metallicum* of different potencies.

Paper-36

Spectroscopic Studies of Metal Complexes of Cu (II), Ni (II), Co (II), Cr (III) and Fe (III) Complexes

Ajit D. Suryawanshi[1], Dhammpal D. Suryawanshi[2], Anjali Rajbhoj[3]

[1]Dept. of Physics, Hon. B. J. College, Ale (Pune) (M.S.)

[2]Dept. of Chemistry, S.C.S. College, Omerga, (Osmanabad)

[3]Dept. of Chemistry, Dr. B. A. M. Univ. Aurangabad

Abstract: 1-(2-Hydroxyphenyl)-3-p-tolylpropane-1,3-dione and its metal complexes have been synthesized by conventional method. The diketone is offered by employing Baker- Venkatraman rearrangement. The synthesized compounds were confirmed by the spectroscopic analysis such as UV, IR, ^{1}H-NMR, ^{13}C-NMR, Mass, Magnetic susceptibility & XRD.

Keywords: Baker-Venkatraman rearrangement, metal complexes, XRD study.

Introduction: The chemistry of 1,3-diketones has attracted the attention of scientists for almost century**[1]**. β-diketones are important class of organic compounds frequently encountered in synthetic chemistry**[2-4]**. They have been used as ligands for coordination of transition metals and have been investigated for use as potential antiviral agents**[5]**. Due to the presence of two oxygen donor atoms and facile keto-enol tautomerism **[6]**, they easily coordinate with metal ions after deprotonating the enolic hydrogen atom and provides stable metal complexes.

Experimental:

Synthesis of 2-acetylphenyl-4-methyl benzoate (A):

To The mixture of 2-hydroxy acetophenone(0.01mol) and 4-methylbenzoic acid (0.01mol), a dry pyridine and $POCl_3$ were added dropwise with constant stirring at 0^{o}C. Then the reaction mixture was stirred for about 7-8 hours. After completion of the reaction, the reaction mixture was poured into 100 ml 1M HCl containing 50 gm of crushed ice and solid obtained was filtered and washed with ice cold water. It was recrystallized from ethanol, filtered and dried.

Synthesis of 1-(2-hydroxyphenyl)-3-p-tolylpropane-1,3-dione (B):

Compound (A) was dissolved in dry pyridine. To this powdered KOH was added and the reaction mixture was stirred for about 3-4 hours. After completion of the reaction, the reaction mixture was poured on ice cold water and acidified with conc. HCl. The yellow solid was filtered off and crystallized from absolute ethanol to obtain pure product.

Spectral study of ligand:

IR study: FT-IR: (KBR) cm^{-1}:3096.25 (OH), 1715.20 (C=O), 1528.16 (Ar C=C).

^{1}H-NMR Study: ^{1}H-NMR (300 MHz, $CDCl_3$-d_6); δ=2.3 (s, 3H, CH_3) 6.8-7 (m, 3H, Ar-H), 7.2-7.4 (m, 3H, Ar-H), 7.5-7.9 (m, 3H, Ar-H). 12.2 (s, 1H, OH), 15.6 (s, 1H, Enolic-OH).

^{13}C-NMR Study:^{13}C-NMR (300MHz, $CDCl_3$); δ=194.1 (s, C-1, C=O), 92.4 (s, C-2, -CH=), 180.2 (s, C-3), 112.5 (s, C-1'), 161.1 (s, C-2'), 117.3 (s, C-3'), 128.4 (d, C-4'), 120.2 (d, C-5'), 126.4 (s, C-6'), 135.4 (d, C-1"), 131.4 (d, C-2",C-6"), 143.1 (s, C-4"), 130.3 (,C-3",C-5"), 22.6 (s,C7",CH_3).

UV/Vis (DMSO)nm: 380,420**. EC-MS**: 255.13 (M+1).

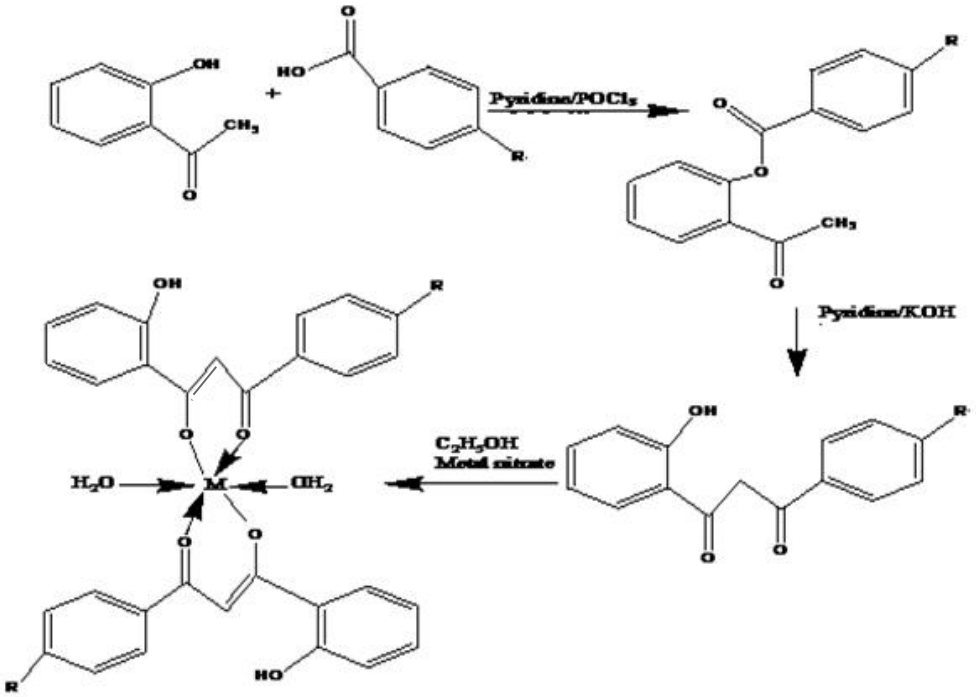

R=Methyl , M= Cu(II), Ni(II), C0(II), Cr(III), Fe(III).

Synthesis of ligand and metal complexes

Results and discussion:

Ester was prepared by the esterification of 2-hydroxyacetophenone with 4-methylbenzoic acid in the presence of $POCl_3$. Ester undergoes Baker-Venkatraman transformation**[7]** to offered pale yellow needle of ligand (B). The decrease in frequency of C=O in complexes suggests the coordination of metal atom with the carbonyl group of ligand **[8].**

Synthesis of metal complexes:

The mixture of compound B and different anhydrous metal nitrates (0.01mol) and 20 ml of anhydrous ethanol were added and refluxed for about 8-9 hrs. The solid particles which precipitated was washed with boiling ethanol and recrystallized from ethyl acetate to give different complexes.

Table I: Molar conductivity, magnetic and Infra-red spectral data of synthesized compounds.

Compound	μ eff (BM)	Molar Conductance	IR (cm^{-1})				
			ν(C=O)	ν(C-O)	ν(-OH)	ν(M-O)	ν(OH) Coordinated H2O Molecule
Ligand			1715	1497	3096	--	---
Cu(II) complex	1.83	20	1690	1501	3116	510	3290
Ni(II) complex	2.62	39	1680	1509	3118	495	3288
Co(II) Complex	4.73	31	1670	1504	3119	524	3286
Cr(III) Complex	4.15	26	1682	1514	3112	518	3270
Fe(III) Complex6.11	5.65	62	1675	1512	3116	505	3275

Powder X-ray diffraction study:

The diffractogram of complex Fe-L_2 shows reflections between 10-62◦. The x-ray diffraction pattern of these complexes with respect to major peaks of relative intensity greater than 10 percent were indexed using a computer programme**[9]**. In concurrence with these cell parameters conditions such as a≠b≠c and α=γ≠β required for a monoclinic sample were tested and found to be satisfactory. Hence, it can be concluded that the Fe(III) complex was monoclinic crystal systems.

Unit cell data and crystal lattice parameter of complex Fe-L:

parameter	**Data**	**Parameter**	**Data**
a(Å)	11.456	Volume (A˚)	628.58

b(Å)	7.562	Density (obs.)	4.07672
c(Å)	7.256	Density (calc.)	4.05320
α(degree)	90	Z	2
β (degree)	101	Space group	$P_{2/m}$
γ(degree)	90	Crystal system	Monoclinic lattice

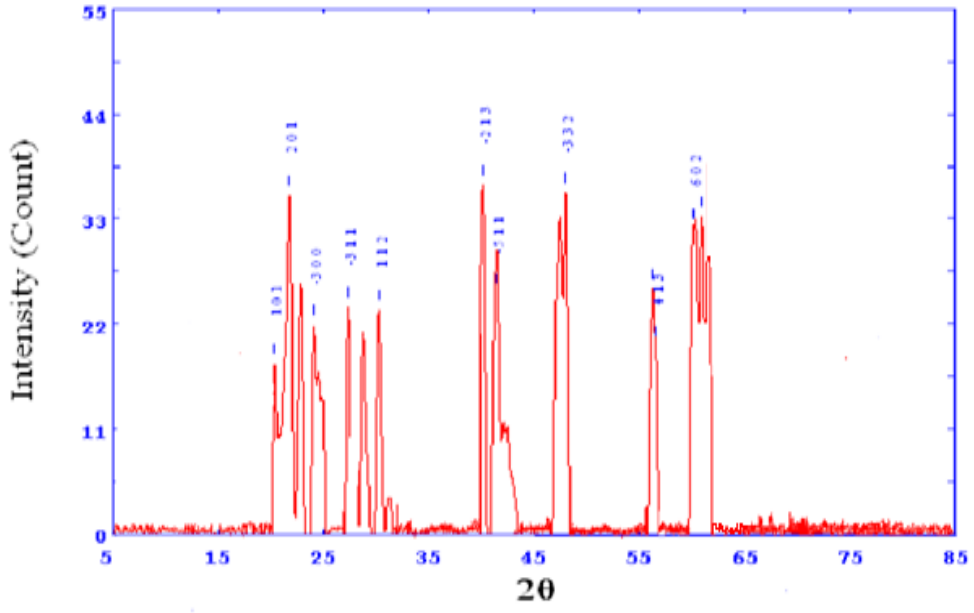

Figure : X-ray diffractogram of Fe-L

Conclusion:

In the present work ligand and its transition metal complexes were synthesized and their structures elucidated on the basis of spectral analysis. ^{1}H-NMR and ^{13}C-NMR spectra revealed that the prepared diketone possess characteristic peaks due to the presence of enolic proton (enol form of β-diketone) and phenolic proton adjacent to carbonyl group. XRD study of Fe-crystal indicates amonoclinic lattice type.

References:

[1] M. Thiyagarajan, S. S. Sharma, Life Sci., 74, (2004), 969.

[2] V. Fargeas, M. Baglouch, E. Muley, J. Baffreau, D. Mehard, P. Gosselin, J. P. Berge, C. Barthomeuf, Tetrahedron, 60, **(2004),** 1035

[3] J. Christoffers, H. Oertling, P. Fisher, W. Frey, Tetrahedron, 59, **(2003),** 3769

[4] A. R. Katritzki, Z. Wang, M. Wang, C. R. Wilkinson, D. Hall, N. G. Akhmedor, J. Org. Chem, 69, **(2004),** 6617

[5] S. Antony, R. Kuttan, G. Kuttam, Immun. Invest**, (1999),** 28, 291

[6] T. Dziemboska, Z. Rozwadowski, Curr. Org. Chem, 5, (2001), 289

[7] R. N. Prasad, M. Agrawal and M. Sharma,J.indian Chem. Soc., 2002, 79:531.

[8] Verma P. N, Sheikh J.I and Juneja H. D., World Applied Sciences Journal, 2011, 14(8):1154.

[9] Carvajal J. R, Roisnel T, Winplotr, A graphic tool for power diffraction, Laboratoire Leon Brillouin (ceal/cnrs) 91191 Gif sur Y vette Cedex, France, 2004.

Paper-37

Investigation of antimicrobial properties and characterization of silver nanoparticles initiated via silver effluent

Savita V. Thakare
Assistant Professor, Department of Chemistry
K.S.K.W. Arts, Science and Commerce College CIDCO Nashik

Abstract

In the current study, developed novel synthesis method for fabrication of silver nanoparticles (Ag NPs) initiated from precursor silver effluent, capping agent PEG400 and reducing agent potassium citrate. Structural characterization of synthesized Ag NPs was done by UV-Visible absorption spectrum, Fourier transforms infrared (FT-IR) and scanning electron microscope (SEM) analysis. Maximum absorption at 430 nm in UV-visible spectrum confirmed Ag NPs synthesis. Morphology of produced particles was studied by SEM image. Purified particles were investigated for presence of antibacterial and antifungal activity.

Keywords

Ag NPs, co-precipitation, UV-Visible, SEM, antimicrobial

Introduction

Nanotechnology is advance science includes research and innovation concerned with assembly and exploitation of new materials and devices on subatomic level [1]. Nanoparticles are being proved as functioning primary building blocks of nanomaterial. The nanoparticles of an extensive scope of materials can be fabricated by number of physical and chemical methods. Some chemical methods cause environmental and health hazards. [2-3]. The green synthesis of silver nanoparticles involves three main steps; selection of solvent medium, selection of environmentally benign reducing agent and selection of non-toxic precursors [4-6]. Green synthesized silver nanoparticle has evolved its potential application in the biomedical field like antibacterial [7-8], biosensor [9-10] and bioimaging [11].

Recently there is diverse antibiotics become inactive against some bacteria and fungi that leads to developed nanoparticles with definite physical, chemical properties have specific antimicrobial activity [12]. Due to the smaller sizes and high amount of surface-area-to-volume ratio of nanoparticles attributed interaction with membranes of viruses, fungi, and bacteria [13]. Researchers have been reported antimicrobial activities of metal nanoparticles like Ag, Cu, Ni, and Co [14-16].

In the present work we report first time the synthesis of silver nanoparticles from gold smith silver effluent as a cheap and abundant source. Potassium citrate is used as the reducing reagent and PEG400 as the capping reagent for gold nanoparticles synthesis. Further examine antimicrobial activity of synthesized silver nanoparticles.

Material and Methods

Silver effluent collected from local goldsmith, PEG400 (Merck Inc.), Potassium citrate (Merck Inc.).

Preparation of silver nanoparticles

20ml Aqueous solution of PEG400 (0.5%) is added to 250ml silver effluent collected from local goldsmith. The mixture was stirred for 30 min to obtain homogenous solution. After these 20 ml of 0.5 M potassium citrate solution of was added to homogenous silver solution and further stirred and refluxed at 60^0C. After 1hr this reaction mixture became turbid indicating the formation of silver nanoparticles. These silver particles were collected by centrifuging the solution at 10000rpm for 10 min. Resulting product was washed with double distilled water and then by 80% alcohol. Resulting product dried at 70^0C and characterised by UV–visible spectroscopic analysis followed by Fourier transform infra-red (FTIR) and scanning electron microscopy (SEM).

Antimicrobial activity of silver nanoparticles

Synthesized starch embedded silver nanoparticles were further analysed for antibacterial and antifungal activity by disc diffusion test against salmonella typhi, klebsiella pneumoniae, staphylococcus aureus and pseudomonas aeruginosa. The disc diffusion test was performed using the standard procedure as described Jorgensen et.al. The inoculums suspension of bacterial strain was swabbed on the entire surface of Luria Bertani agar surface. Sterile 6mm filter paper disc was aseptically placed on LB agar surface. Sterile disc was soaked in synthesized silver nanoparticle solution for 30 min. After 30 min, disc was placed on L.B plate. The plates were left at ambient temperature for 15 min to allow excess prediffusion of solution prior to incubation at 37^0C for 24 hrs. After incubation Inhibition zones were measured.

Results and Discussion

Fig.1 UV–Visible absorption spectra of reaction mixture shows characteristic λmax for Ag NPs. In spectrum a single strong peak with a maximum around 430 nm was observed.

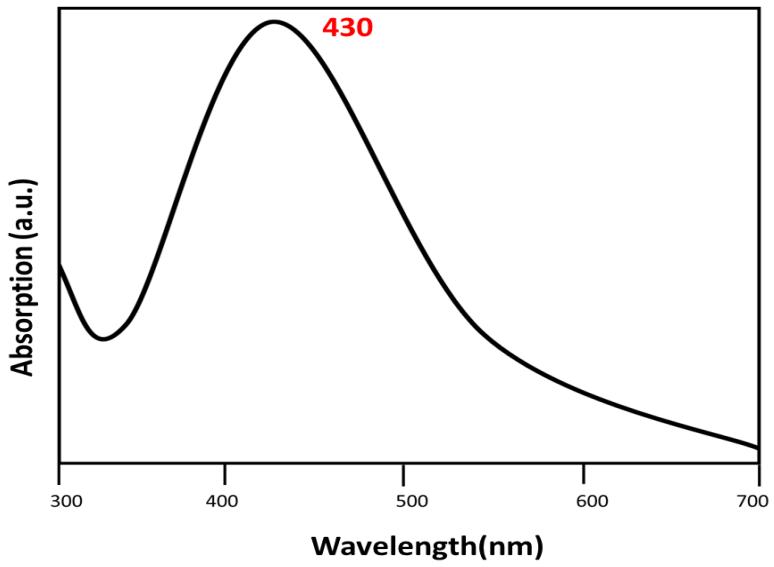

Figure.1 UV spectrum of silver nanoparticles

Fig.2 depicts FT-IR spectrum of Ag nanoparticles was recorded in solid phase using KBr pellet technique in the range of 400-4000 cm-1. The FTIR spectrum of silver nanoparticle shows the absorption bands at 3676 $cm^{-1}$was due to the O–H stretching band and characteristic absorption band at bands at 1270 and 1030 cm^{-1} due to C–O, C–O–C stretches and C–O–H bends vibrations of Ag NPs in PEG. 1400 and 1344 cm^{-1} were due to C–H bending vibrations in the aliphatic C–H group.

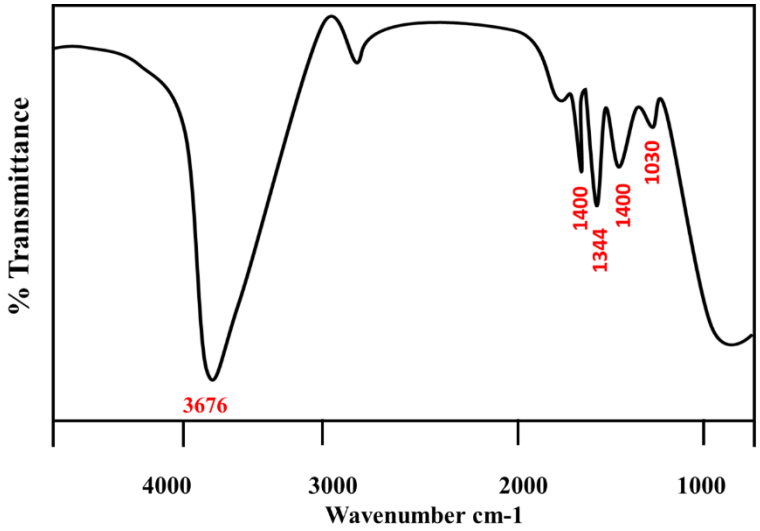

Figure.2 FT-IR spectrum of silver nanoparticles

The scanning electron micrographs of PEG 400 capped Ag-NPs Fig.3 shows homogenous and rod like porous surface structures.

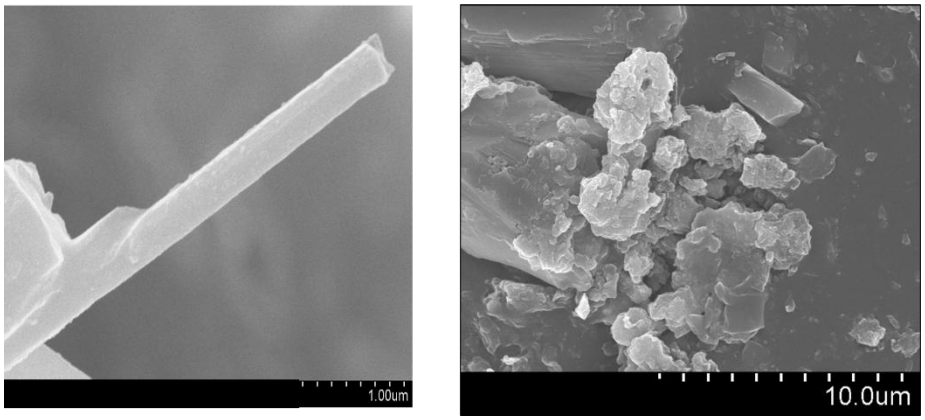

Figure.4 SEM of silver nanoparticles

Anti-microbial activity was checked for synthesized silver nanoparticles and better results were obtained for Pseudomonas aeruginosa and Rhizopus Fig.4. Antibacterial activity of silver nanoparticles was observed as zone of inhibition shown in table 1. Silver nanoparticle solution was inhibited growth of all selected bacteria and fungi.

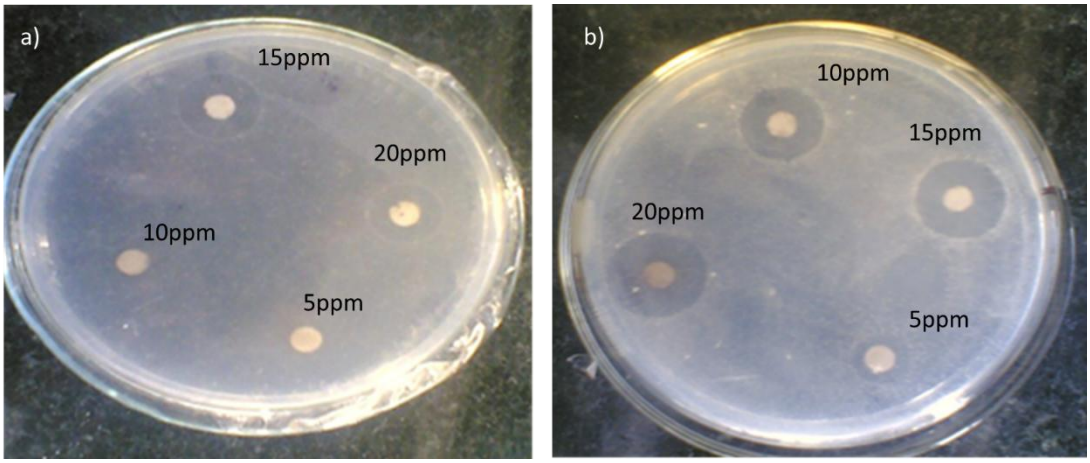

Figure 4. Antimicrobial activity of silver nanoparticles against a) Pseudomonas aeruginosa b) Rhizopus

	5ppm	10 ppm	15ppm	20ppm
Name of bacteria	Zone of inhibition (diameter in mm)			
Pseudomonas aeruginosa	12mm	23mm	28mm	32mm
Salmonella typhi	11mm	15mm	22mm	23mm
Staphylococcus aureus	-	03mm	04mm	07mm
Klebsiella	-	-	9mm	16mm
Name of fungus				
Rhizopus	12mm	19mm	20mm	35mm
Candida albicans	14mm	17mm	25mm	27mm
Aspergillus niger	-	7mm	9mm	16mm

*1ppm silver nanoparticle solution was prepared by dissolving 1miligram of silver nanoparticle powder in 1000ml of double distilled deionized water

Conclusion

Green synthesis of nanoparticles is reported by many ways. Present investigation utilizes potassium citrate as reducing agents, PEG 400 as capping agent and first time goldsmith silver effluent is used as a green source for synthesis of silver nanoparticles is reported. Samples showed maximum absorbance at 430 nm hence confirmed presence of Ag NPs. FTIR spectrum showed significant peaks indicating formation of PEG 400 capped Ag NPs. SEM images confirmed morphology of nano particles. Synthesized nanoparticles shown antibacterial activity against Pseudomonas aeruginosa, Salmonella typhi, Staphylococcus aureus, Klebsiella and antifungal activity against Rhizopus, Candida albicans and Aspergillus niger.

References

1. Porter A. L., Youtie J., Shapira P., Schoeneck D. J., Refining search terms for nanotechnology, J Nanopart Res. 10 (2008)715–728.

2. Ahmed S., Ahmad M., Swami B.L, Ikram S., A review on plants extract mediated synthesis of silver nanoparticles for antimicrobial applications: a green expertise. J Adv Res 5(2016)17–28.
3. Zhang X.F., Liu ZG, Shen W, Gurunathan S., Silver nanoparticles: synthesis, characterization, properties, applications, and therapeutic approaches. Int J Mol Sci 17(2016)E1534.
4. Jongnam P., Jin J., Soon G. K., Youngjin J., Taeghwan H. Synthesis of monodisperse spherical nanocrystals, Angew Chem Int Ed Engl.,46(2007)4630-60.
5. Lu A.H., Salabas E. L., Schüth F., Magnetic Nanoparticles: Synthesis, Protection, Functionalization, and Application. Angewandte Chemie International Edition, 46(2007)1222–1244.
6. Soloviev M., Nanobiotechnology today: focus on nanoparticles, J. Nanobiotechnology, 5(2007), 11.
7. Sharma V. K., Yngard R. A., Lin Y., Silver nanoparticles: Green synthesis and their antimicrobial activities, Advances in Colloid and Interface Science, 145(2009)83–96.
8. Zargar M., Hamid A.A., Bakar F.B., Shamsudin M.N., Shameli K., Jahanshiri F., Farahani F., Green synthesis and antibacterial effect of silver nanoparticles using Vitex negundo L., Molecules, 16(2011)6667–6676.
9. Zhang X., Guo Q., Cui D., Recent Advances in Nanotechnology Applied to Biosensors. Sensors, 9(2009)1033–1053.
10. Zhang Y., Zhang K., Ma H., Electrochemical DNA biosensor based on silver nanoparticles/poly(3-(3-pyridyl) acrylic acid)/carbon nanotubes modified electrode. Anal. Biochem.,387(2009) 13–19.
11. Zheng J., Ding Y., Tian B., Wang Z.L., Zhuang X., Luminescent and raman active silver nanoparticles with polycrystalline structure, J. Am. Chem. Soc.,130(2008)10472–10473.
12. Pankhurst Q. A., Thanh N. K. T., Jones S. K., DobsonJ.,Progress in applications of magnetic nanoparticles in biomedicine, Journal of Physics D: Applied Physics, 42(2009) 1–13.
13. Morones J. R., Elechiguerra J. L., Camacho A.et al., The bactericidal effect of silver nanoparticles, Nanotechnology, 16(2005)2346–2353.
14. Ravikumar S., Gokulakrishnan R., Boomi P., In vitro antibacterial activity of the metal oxide nanoparticles against urinary tract infectious bacterial pathogens, Asian Pacific Journal of Tropical Disease, 2 (2012) 85–89.
15. Patra C. R., Bhattacharya R., Mukhopadhyay D., Mukherjee P., Fabrication of gold nanoparticles for targeted therapy in pancreatic cancer. Advanced Drug Delivery Reviews, 62((2010)346–361.
16. Xing M., Ge L., Wang M., Li, Q., Li X.,Ouyang J., Nanosilver particles in medical applications: synthesis, performance, and toxicity, Int. J. Nanomedicine, 6(2014)2399-407.

Paper-38

STUDIES ON GLYCOGEN CONTENT AND HAEMOLYMPH LIPID PROFILE IN FRESHWATER CRAB, *BARYTELPHUSA GUERINI* IN RELATION TO REPRODUCTION

Bhausaheb R Ghorpade

Dept. of Zoology, Shri Anand College, Pathardi Dist. Ahmednagar

ABSTRACT:

The present study was undertaken to access the reproductive cycle, glycogen content and haemolymph lipid profile of the freshwater crab, *Barytelphusa guerini*, during different reproductive seasons of the year. The freshwater crabs are available abundantly in lakes and ponds of study area, the live freshwater crabs *Barytelphusa guerini* were collected from Nathsagar dam, Paithan, Dist. Aurangabad (M.S.) for the period January to December 2019. The glycogen content in gonads and hepatopancreas in relation to reproduction was studied during different reproductive seasons. Study showed that during maturation, glycogen content increased in the gonads and decreased in hepatopancreas. During preparatory phase glycogen were higher in gonad and hepatopancreas. The reproductive cycle and glycogen content in gonads and hepatopancreas was studied during different months of the year.

Key words: - *Barytelphusa guerini*, haemolymph, reproductive stage, glycogen content, lipid profile.

INTRODUCTION:

The decapod crustaceans are commercially important as they are with high nutritional contents. Crabs are commercially important and command high price as there is a rapidly expanding demand for crab meat both in local and international markets. Crab has a unique and delicious taste as compared with fish and mollusc. *Barytelphusa guerini* is most popular because of its size, meat quality and it is consumed largely as a protein source. Reproduction is the main mechanism that keeps species continuity so that it contributes to regulate the population size. Biochemical composition of the gonads and whole body in relation to reproductive cycle has been studied in some species of prawns and crabs.

Glycogen is the main constituent of the food of many crustaceans. Tissue carbohydrate in the form of glucose and glycogen serve as important source of food energy with vital

activities. Mucopolysaccharides and glycoproteins provide mechanical and protective support during maturation of gonads (Nayab Ansari, 2013). In crustaceans the somatic growth and gametogenesis are two high-energy consuming physiological events. The utilization of hepatopancreatic lipid has been documented for somatic growth. During reproductive seasons lipids along with some other biochemical are channelled towards the gonads to meet the cost of active gametogenesis in crustaceans. While studying the seasonal changes in organic composition, the lipid content exhibited the most pronounced seasonal changes (Lubzens et al., 1995). In freshwater crabs, studied so far, Kengar, (1998) and Ansari (2001) in *Barytelphusa guerini* and *Barytelphusacunicularis* lipid appeared to be the major reserve during, reproductive cycle.

The origin of lipids reaching the ovary is not fully understood. It is not known whether these lipids pass viathe metabolic junction in the hepatopancreas or are taken up directly from the gut. Lipids stored in the hepatopancreas have been shown to be transported to the ovary during vitellogenesis (Harrison, 1990). However, the amount of lipids accumulated within the ovaries is greater than that stored in the hepatopancreas (Castille and Lawrence, 1989). In most species, PLs, TAGs and sterols are the most abundant ovarian lipid classes. In the blue crab, *Callinectessapidus*, lipid droplet, which form a minor component in immature ovaries, constitute 27 % of the total lipids in mature ovaries (Lee and Walker, 1995). Mourente et al., (1994) indicated that the midgut gland (the hepatopancreas) and ovarian cells have a limited capacity to convert linoleic and linolenic acids so requirement is from the diet. Being insoluble in water, lipids are transported as lipoproteins in the haemolymph. So far, three lipoproteins have been identified and isolated from crustacean haemolymph, all belonging to the high-density lipoprotein (HDL) and very high-density lipoprotein (VHDL) classes. The VHDL fraction was found to contain the clotting protein (Hall et al., 1995). Lee and Puppione (2005) isolated and characterized two different high density lipoproteins in the haemolymph of blue crab, *Callinectessapidus*.

MATERIALS AND METHODS:

For the present study the live freshwater crabs *Barytelphusa guerini* were collected from Nathsagar dam, Paithan, Dist. Aurangabad (M.S.) for the period January to December 2019. They are abundantly available in all seasons of the year. The crabs were kept separately in aerated water in glass aquarium. They were acclimatized to laboratory conditions for three days before carrying out the biochemical analysis experiment. The water was changed thrice

daily and continuous aeration was provided. The crabs were fed with earthworms or small pieces of goat meat.

For estimation of glycogen, the method recommended by Kemp, et al. (1954) was employed using Engel's Colorimeter. The amount of glycogen was calculated by multiplying the glucose value by the factor 0.927.Haemolymph from male and female *Barytelphusa guerini*was obtained by making a cut in the anterior rostrum and collected haemolymph into 10% sodium citrate solution to avoid clotting. Fractionations of haemolymph into high-density lipoproteins (HDL), low density lipoproteins (LDL), very low-density lipoproteins (VLDL) were assayed on fully automated analyser (ECHO Italy).

RESULTS

The results are presented in the Figs.1-2; clearly reveal a marked biochemical change in the ovary, testes and hepatopancreas of *Barytelphusa guerini.*

Glycogen:

The glycogen content in the gonads and hepatopancreas were estimated monthly for the year 2019. The glycogen content in case of testis was within the range of 33.21to65.90 µg/gm, whereas, in ovary, it ranged from 33.62 to 68.2µg/gm. The data obtained during the year shows certain seasonal changes in glycogen contents of the male and female gonads especially during the breeding season. There was a significant decrease in glycogen content during the spawning period i.e. June to September. In testis, higher glycogen content was found in the month of May (65.90), whereas in hepatopancreas highest and lowest glycogen content was found in the month April (94.82) and August (42.38) respectively. The highest glycogen content in *Barytelphusa guerini* ovary was found in the month of April 2019 (68.2%) and lowest was found in the month of June 2019 (33.62%). During the resting stage or post reproductive season i.e. September to December, there is a little consistency in the glycogen content of the gonad. During the preparatory period or ripening period of the gonad i.e. January to April, the percentage of glycogen was increased. Total glycogen content in different tissues of crab Barytelphusa guerini shows variations from season to season. The seasonal analysis of glycogen content in different body tissues of *Barytelphusa guerini* and results are given in table-1 and illustrated in fig. 1.

Table 1 Seasonal change in glycogen content in hepatopancreas, ovary and testis of *Barytelphusa guerini* for the period January to December 2019

Month	Hepatopancreas glycogen Average(µg/gm) ± SD	Ovary glycogen Average(µg/gm) ± SD	Testes glycogen Average(µg/gm) ± SD
January	79.22±7.64	56.76±5.74	54.51±6.78
February	86.12±6.67	55.82±5.62	55.71±6.82
March	90.54±7.82	67.12±5.92	63.42±6.96
April	94.82±6.74	68.2±6.72	64.89±6.8
May	84.66±6.63	63.18±6.62	65.90±5.72
June	49.24±4.42	33.62±4.73	45.73±4.84
July	43.60±4.24	33.64±4.66	44.24±4.74
August	42.38±4.16	34.70±3.90	33.21±3.32
September	67.32±5.34	44.82±4.53	42.16±4.24
October	68.32±5.44	55.24±4.64	52.19±4.36
November	72.24±6.56	56.78±4.78	53.39±4.6
December	76.78±6.36	56.70±4.76	53.42±4.62

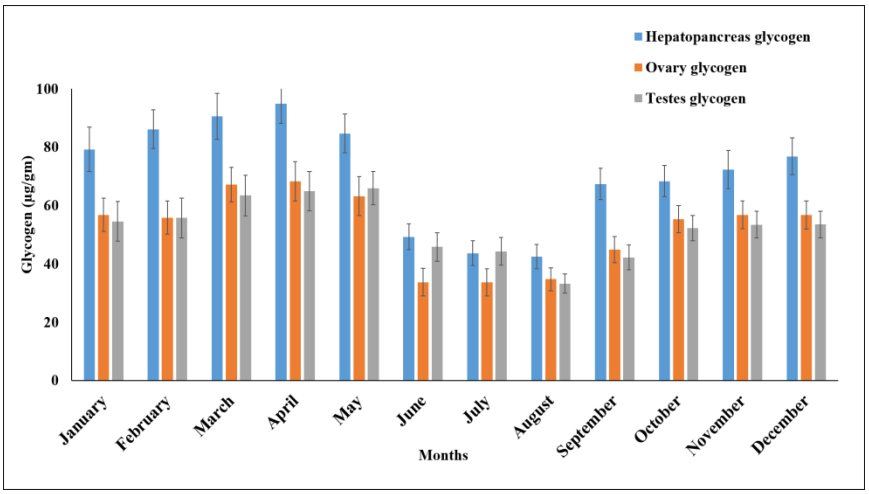

Figure: 1 Frequency histogram showing mean percentage of glycogen content in hepatopancreas and gonads of *Barytelphusa guerini* for the period January to December 2019

Lipid profile

Cholesterol, triglycerides and lipoproteins are the main lipid classes found in haemolymph of *Barytelphusa guerini*. The haemolymph lipid profile of male and female crab has shown variation during different reproductive periods. The lipid profile of haemolymph in vitellogenic female and mature male are shown in table-2 and Fig.2.

Table 2: Lipid profile in haemolymph of *Barytelphusa guerini*

Sr. No	Lipid	vitellogenic female (Qty mg/dI)	Matured male (Qty mg/dI)
1	Cholesterol	43	59
2	Triglycerides	55	76
3	HDL (Direct)	14	13
4	LDL	18	30
5	VLDL	12	16
6	Total : HDL ratio	3:0	4:7

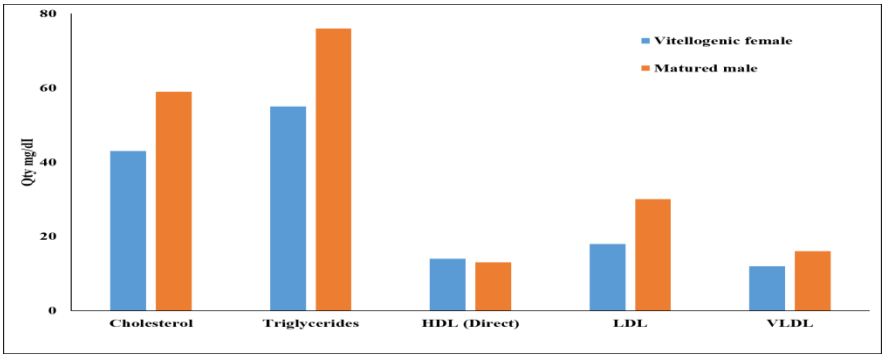

Fig-2 Changes in the lipid profile in haemolymph of female and male crab, *Barytelphusa guerini*

DISCUSSION:

The amount of stored biochemical components in the body is greatly influenced by the state of activity and breeding of animals (Nayab Ansari, 2013). It is known that the hepatopancreas serves as a storage organ, the principal storage nutrients being fat and glycogen. It is further suggested that the organic material may be transferred from the storage organ to gonad as the animal matures. A striking change in the glycogen level was seen during the course of reproductive cycle in testis and ovary. The level reached lowest value at the time of spawning period and after spawning the level was increased till the complete growth of the gonad. Vaishali Gangotri (2016) suggested that the stored glycogen might be utilised for the formation of reproductive elements and this counts for the decrease in the glycogen content during the breeding season. Similar observations are made by Diwan and

Nagabhushanam, (1974) in *Barytelphusa cunicularis*. This clears that the glycogen shows seasonal variations in its content in association with the sexual and metabolic activity.

Phospholipids (PLs), sterols, triacylglycerols (TAGs) and diacylglycerols (DAGs) are the main lipid classes found in marine shrimps and are associated with the maturation of oocytes and the survival of the initial larval stages (Xu et al., 1993). Haemolymph lipoproteins carry mainly phospholipids in HDL (high density lipoproteins). Lubzens et al., (1997), previously shown that female HDL is composed of two lipoproteins: LP1 and vitellogenin. The vitellogenin contains phospholipids, diacylglycerides and cholesterol. Triacylglycerides are found almost exclusively in vitellogenin. Vitellogenin (vg), is a female specific protein circulating in the haemolymph, is the precursor of vitellin that is the nutritive material necessary for the development of an embryo (Ying Nan Chen et al., 1998). The cholesterol, lipoproteins and triglycerides were the main lipid classes observed in haemolymph of crab, *Barytelphusa guerini*.

In the present study it was found that haemolymph of vitellogenic female shown decreased proportion of HDL as compared to nonvitellogenic female. The relative proportion of HDLs decreased during the course of vitellogenesis, while that of triglycerides are increased. The increase in amount of lipid fractions as maturation proceeds reflects the accumulation vitellin during ovarian maturation. Similar data have been reported previously for the lipid composition of purified vitellin (Lubzens et al., 1997) in marine shrimp *Penaeussemisulcatus.*In crayfish, *Parastacusvaricosus* haemolymph, Daiana da Silva et al., (2007) observed significant variation only in cholesterol and lipid levels. Shirley et al., (2008) reported that VLDL increases to maximum level during vitellogenesis in ovary of shrimp.

ACKNOWLEDGEMENT:

I am thankful to Principal Shri Anand College, Pathardi for providing necessary laboratories facilities to carry out present work.

REFERENCES

1. **Ansari, N T (2001)** Protein patterns in freshwater crabs. Ph.D. Thesis Marathwada University, Aurangabad.
2. **Castille, F. C. and Lawrence, A. L. (1989)**The relationship between maturation and biochemical composition of the gonads and digestive glands of the shrimps *Penaeus aztecus* lves and *Penaeus setiferus* (L.). *J. Crust. Biol*. 9: 202-211.

3. **Daiana, D. S., Castiglioni, B. K. D., Guendalina, T. O. and Georgina, B. B. (2007)** Seasonal variations in the intermediate metabolism of *Parastacusvaricosus*(Crustacea, Decapoda, Parastacidae) *Comparative Biochemistry and Physiology*, 148(1): 204-213.
4. **Diwan, A.D. and Nagabhushanam, R. (1974)** Reproductive cycle and Biochemical changes in the gonads of the freshwater crab, Barytelphusa Cunicularis, (Westwood), Indian. J. Fish., 21 (1): 164-176.Hall et al., 1995
5. **Harrison, K.E. (1990):** The role of nutrition in maturation, reproduction and embryonic development of decapod crustaceans: a review. Journal of Shellfish Research 9(9):1-28
6. **Kemp, A., Van Kits and Heijmingen, A.I.M. (1954)** A Colorimetric method for the determination of glycogen in tissues, Biochem. J., 54: 646.
7. **Kengar S B (1998)**Ecophysiological studies in freshwater crab, *Barytelphusa guerini*. Ph.D. thesis, Marathwada University, Aurangabad, M. S.
8. **Lee Richard F, Donald L Puppione, (2005)** Lipoproteins I and II from the hemolymph of the blue crab *Callinectessapidus*: Lipoprotein II associated with vitellogenesis. J. of Experimental Zoology, 248(3): 278-289
9. **Lee, R. F. and Walker, A. (1995)**Lipovitellin and lipid droplet accumulation in oocytes during ovarian maturation in the blue crab, *Callinectessapidus*. *J. Exp. Zool*, 271: 401-412.
10. **Lubzens, E M, Khayat, Ravid, T Funkenstein B and Tietz, A (1995)** Lipoproteins and lipid accumulation within the ovaries of penaeid shrimp. Israeli Journal of Aquaculture Bamidgeh 47 (3-4): 185-195
11. **Lubzens, E., Ravid, T., Khayat, M., Daube, N. And Tietz, A.(1997)** Isolation and characterization of the high density lipoproteins from the hemolymph and ovary of the penaeid shrimp *Penaeussemisulcatus* (de Haan): apoproteins and lipids. *J ExpZool* 278: 339-348.
12. **Mourente - A Medina, S Gonzfilez, A Rodrfguez (1994)** Changes in lipid class and fatty acid contents in the ovary and midgut gland of the female fiddler crab *Ucatangeri* (Decapoda, Ocypodidae) during maturation Marine Biology 121:187-197
13. **Nayab Ansari (2013)** Seasonal Variation In the glycogen content of freshwater Crabs: Barytelphusa Cunicularis and Barytelphusa guerini during Different Seasons. International Journal of Advancements in Research & Technology, Volume 2, Issue5, 225 ISSN: 2278-7763
14. **Shirley, H., Kwan T., John B.and Siu-Ming C. (2008)** From hepatopancreas to ovary: Molecular characterization of a shrimp processing of vitellogenin. *Biol. Reproduction*: 18218613.

15. **Vaishali Gangotri (2016)** Reproductive Cycle and Biochemical Changes in the Gonads of the Freshwater Crab, Barytelphusa guerini H. Milne Edwards) (Decapoda, Potamidea). International Journal of Current Research Vol. 8, Issue, 09, ISSN: 0975-833X pp.37796-37800
16. **Xu, X. L, Ji, W. J, Castell, J. D. and O' Dor, R. K, (1993)**The nutritional value of dietary n-3 and n-6 fatty acids for the Chinese prawn. *Aquaculture,* 118: 277-285.
17. **Chen, Y. N. and Kuo, C.M. (1998)** Purification and characterization of vitellin from the freshwater giant prawn, *Microbrachium rosenbergii* Zoological *Studies* 37(2): 126-136.

Paper-39

Development of metal oxide semiconductor gas sensor based system (E-Nose) for tropical fruit sorting

Ashok Kanade[1] and Arvind Shaligram[2]

[1]*Department of Electronic Science, P.V.P. College, Pravaranagar, India*

[2]*Department of Electronic-Science, Savitribai Phule Pune University, Pune, India*

Abstract

The present work deals with development of electronic Nose using commercially available metal oxide gas sensor array having wise spectrum of VOC combustible gas sensing. The sensor used are non-selective to specific gas as like gas sensing receptors in mammalian nostril. The developed system consists of hardware and software for pattern recognition. The developed systems performance was evaluated for pre-packaging classification of guava fruit nondestructively. Radar plot and principal component analysis (PCA) techniques were used in order to investigate the effectiveness of developed e-nose system for discriminating guava fruit samples in four different ripening states as green, ripe, overripe and spoiled. The radar plot shows different odor signature for different ripening states. The Principle component analysis plot indicates a distinct separation between the four classes. The results suggest that this e-nose system is capable to classify guava fruits and it would be a feasible system to be used in a real scenario.

Keywords: *Electronic Nose, Guava fruit, Fruit classification, PCA, Fruit sorting*

1. Introduction

Packaging of harvested fruits and vegetables is important step in journey from producer to consumer. The handling, transporting and marketing of fresh produce is practiced through bags, crates, baskets, hampers, cartons, bulk bins and palletized containers. The permeability requirement depends upon respiration rate, package bulk density and temperature of the storage. The pre-packaging classification reduces the transportation cost by eliminating unwanted and inedible portion of fruit. Pre-packaging reduces the shopping time of the consumer as the produce is graded before the package. By predicting shelf life at room temperature and refrigerated conditions, pre-packaging helps the grocer to market his produce over a long period and thereby, avoid losses due to spoilage [1].Conventionally guava fruits classification before packaging has been done by trained human graders according to odor and skin color. But this approach has many disadvantages in terms of objectivity and repeatability. Also a human nose cannot sniff high number of samples because it gets fatigues rapidly with increasing number of samples and also there is possibility of eye disease like color blindness etc. [2]. The failure rate in human grader based classification can be avoided by using electronic classification systems. The electronic classification systems are either destructive or nondestructive types [3]. The conventional fruit classification methods are destructive type in which fruit need to puncture, crush or sliced. In some methods chemicals were applied on fruits for classification, which may danger to human health. Hence such methods are not desirable. For testing firmness of a fruit, a slicing and puncture through Penetrometer will damage the fruit resulting in spoilt produce. Other methods include measuring levels of chemical species; pH, TSS, TTA, ethylene

contents, high performance liquid chromatography or gas chromatography-mass spectrometry (GC–MS) requires crushing of fruit for getting pulp or juice [4]. Besides these destructive conventional methods, there are also non destructive techniques which are used. These methods include NMR, PMR, vision system and acoustics. However, all above conventional methods for classification of guava are inconvenient and complicated because they requires specialized skills, are time intensive, labour and are more costly. A simple and reliable method for classification of guava fruits is therefore needed.

Another popular non destructive method for fruit classification is the use of electronic nose. An e-nose system, which is a simple and fast method using a specially designed gas sensors array and suitable pattern recognition techniques to detect and discriminate between complex fruit odors [5].

This paper presents here, how we developed a low-cost application specific portable e-nose system and tests its ability for classification of guava fruit cultivar compared to conventional methods. The classification results confirmed that the developed e-nose system is effective and can tackles many problems associated with the use of human panels. Individual variability, mental state, adaptation, fatigue, infections, subjectivity and exposure to hazardous compounds all parameter taken for consideration. The e-nose can create odor exposure profiles beyond the capabilities of the human panel or GC/MS measurement techniques [6-7]. Consider the demands of multi-target contaminants detection and the low-cost of e-nose, we select eight Figaro Inc. in Japan made TGSxx series MOS gas sensors. The TGSxx series sensors were selected because they have cost-effective, cross sensitive. The main objectives in this study were (1) Evaluate the capacity to measure the change in VOC production of guava fruit during different ripening states in controlled environment using a developed electronic nose device in our laboratory (2) Study Radar plot analysis and principal component analysis (PCA) to obtain whether the developed electronic nose system is able to discriminate between different ripening classes of guava fruits (3)To check prediction performance of developed e-nose system to unknown guava fruit samples using feed forward neural network with back propagation training algorithm.

2. Materials and methods

2.1 Design of electronic nose using MOS gas sensors

Figure 1 shows schematic diagram of developed e-nose system that was used for the experimentation. The developed electronic nose system consisting of four functional components that operates serially on an odorant sample; a fruit sample handler called as concentration chamber, an array of eight different MOS gas sensors, a signal conditioning unit and DAQ card connected to laptop which has indigenously developed GUI for data acquisition and pre-processing programmed in LabVIEW2012 software.

The most crucial part of the e-nose is the odor delivery system. The purpose of this system is to transfer the headspace or VOC released by fruit to be analyzed to the gas sensors array. The odor delivery system is designed to measure static response of gas sensor array.

The sensor array is composed of eight metal oxide semiconductor (n-MOS) type chemical sensors. Commercially available tin oxide gas sensors made from Figaro Inc. Japan

were chosen to form the chemical sensor array. Table 1 specifies the sensors used in the array and their primary target application gases.

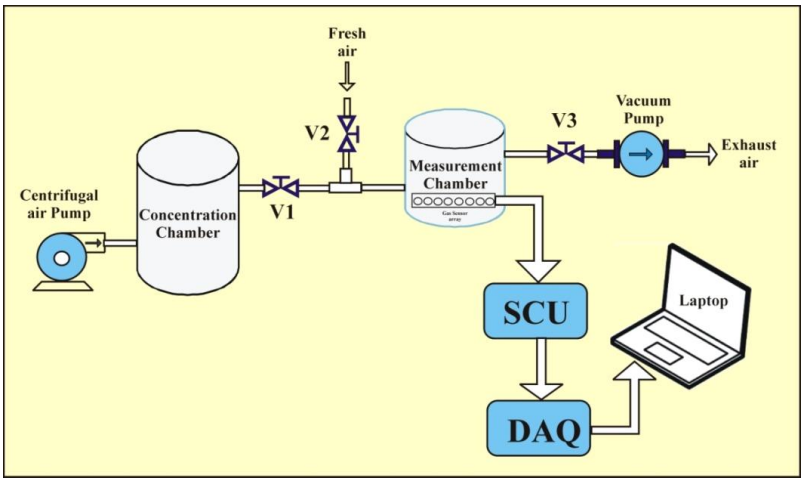

Figure 1: Schematic diagram of developed E-nose system.

The MOS sensors conductivity changes due to adsorption of molecules in the gas phase, and on subsequent surface reactions. They consist of a ceramic substrate coated by a metal oxide semiconducting film, and heated by a wire resistor. These sensors show a certain degree of affinity towards a specific gas but are sensitive towards a wide spectrum of gas types with overlapping sensitivities. These sensors housed in a stainless steel sensor chamber.

Table 2: E-nose Array sensors and their application gases

Sensor No.	Sensor Model	Target Gas Sensitivity
1,3	TGS2602	VOCs, ammonia, H2S, etc
2	TGS2600	hydrogen, ethanol, etc.
4	TGS2611	Methane
5	TGS2620	Alcohol, Solvent vapors
6	TGS822	Organic Solvent Vapors
7	TGS813	LPG, Methane
8	TGS832	Chlorofluorocarbon

The measuring circuit of each sensor is shown in fig.2. A load resistor is connected in series with each sensor and a common power supply of 5 V is used for both the heater voltage and the voltage applied to the voltage divider formed by the sensors and the load resistances. The voltage across the load resistor was used as response of the sensor.

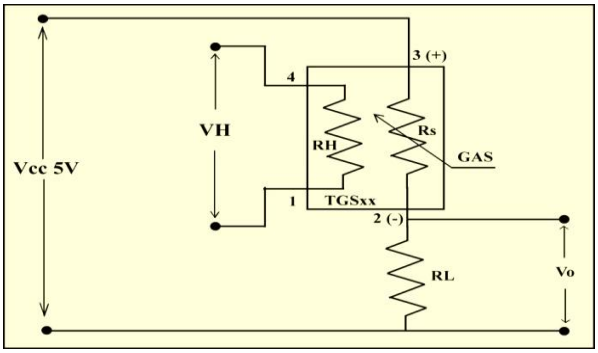

Figure 2: Unit cell circuit diagram of e-nose sensor array

The relationship between sensor resistance and the concentration of deoxidizing gas can be expressed by the following equation over a certain range of gas concentration:

$$Rs = A[C]^{-\alpha} \quad (1)$$

Where:

Rs = electrical resistance of the sensor

A = constant

[C] = gas concentration

α = slope of Rs curve

2.2 Software for Data acquisition and analysis

The national instruments USB6009 DAQ card and specially developed software GUI for data acquisition was used. DAQ cards 8 analog inputs Channels (A0-A7) were used to acquire analog signals from the sensor array. Developed electronic nose requires various activities for its operation. Many of these activities are repetitive actions that must be scheduled at fixed time intervals. Figure 3 shows a flow diagram representing all the actions necessary to perform a complete measurement cycle

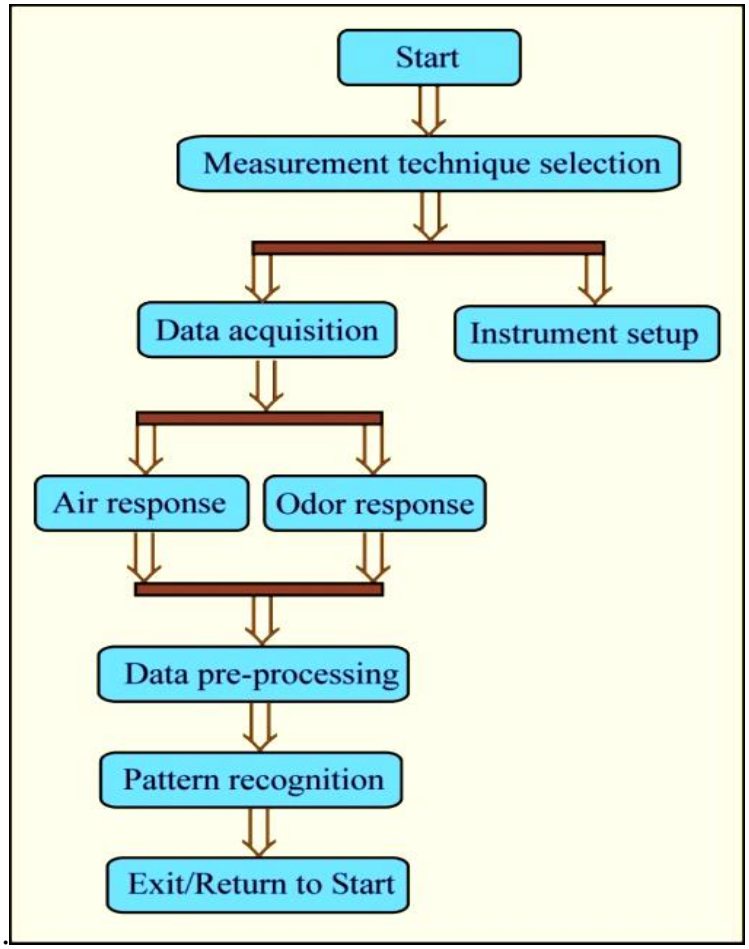

Figure 3: Macro activities in developed e-nose system operation

A complete library of VIs for data acquisition, signal pre-processing, storage, feature extraction, normalization and pattern

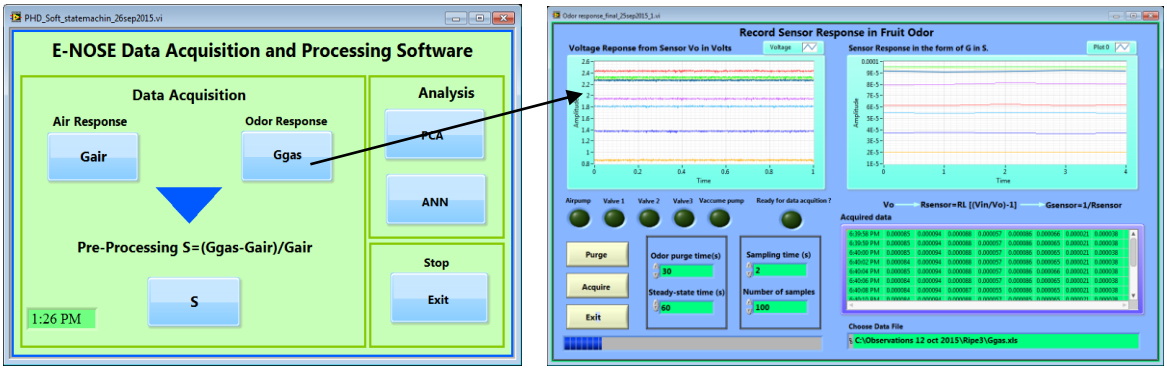

recognition, instrument control are contained in the developed e-nose software tool. This software is based on state machine technology and programmed in LabVIEW2012. Particular states are available to user for do specific work. Individual buttons are provided for the particular operation on the main menu VI as shown in Figure 4a. An Exit or Back button on each VI is provided to return to the main menu VI.

(a)

(b)

Figure 4: a) E-Nose Software main user interface b) Data acquisition interface for odor

In main user interface, user first record the sensor response in air then record the sensor response in odor gas and finally do the pre-processing on stored data. The pre-processed data will be saving for analysis and pattern recognition purpose. The PCA is available for pattern recognition statistically. The user has choice to enter number of samples and sampling time in seconds. The acquired data displayed on waveform graph as time Vs sensor response as shown in fig. 5b. In calibration the voltage response was converted into change in conductance of sensor (G) using below formulas. (2-5)

$$Vo = \frac{RL}{RL+Rs} * Vcc \qquad \text{.....(2)}$$

[Vcc=5V constant, RL=10K constant, Vo =Sensor response in V]

$$Rs = RL\left[\frac{Vcc}{Vo} - 1\right] \qquad \text{..... (3)}$$

Rs=sensor resistance in Ω

$$G = \frac{1}{Rs} \qquad \text{..... (4)}$$

[G=Conductance of sensor in Siemens]

Thus sensor array data was calibrated and converted into sensor conductance. After calibration the eight channel data was collected in the form of matrix array and stored in an excel sheet for further processing. The acquired sensor responses were displayed with color codes as voltage and conductance with respect to time on the front panel of VI as shown in fig.4b. The numerical value of the acquired data at a particular instant was also displayed.

Each sensor produces a steady state response which evolves, as the target odor vapor exposed to the sensor array. There are several interfering inputs which affect the responses of the sensor. Drift problem occurs in the pre-processing and the recognition stage .The standard methods applied for data preprocessing is relative response (S) to a target odor. The separate VI is developed for pre-processing accessible from main user interface.

The relative response (S) to a target gas is defined as the ratio of the change in conductance of a sample upon exposure of the gas to the original conductance in air. The relation for S is given as

$$S = \frac{Ggas - Gair}{Gair} \qquad (5)$$

Where:
S=Relative response of sensor,
Ggas=Conductance of sensor in gas environment, (ref.exp.4)
Gair=Conductance of sensor in air environment.
Specificity or selectivity is defined as the ability of a sensor to respond to a certain gas in the presence of different gases.

2.3 Experimental design

The Guava (*Psidium guajava*) fruits of Lucknow 49 type were obtained from the orchard at altitude 504 m, latitude 19.76° north, longitude 74.48° east. Fruits were selected for uniformity of size, color and freedom from blemishes. The trained human grader's service was used for picking the fruit from tree and sorting into four classes as green, ripe, overripe and spoiled. These fruits were selected and sorted according to uniform size, weight and color approximately. The harvested fruits were washed under clean running water and immersed in a 1% sodium hypochlorite solution at 25 °C for 5 minutes for disinfection. After drying the fruits were placed in carton boxes. After drying, the storage was conducted in laboratory condition having controlled environment maintained at a temperature and relative humidity of 26 ± 1 °C and 41 ± 5% respectively.

The experimental design used was completely random (CRD), with 2 treatments to each fruit sample. The experiment consisted of 10 repetitions for each treatment. For training 15 fruits samples of each class were used and it resulted in 300 observations for each class and total 1200 observations for four classes of guava fruit. For validation of trained ANN, 5 fruits samples in each class were used and it resulted into 100 observations per class. All four different ripening state fruits were evaluated at the picked day (day 0) using developed electronic nose technique.

2.4 Fruit odor analysis procedure using developed hardware and software

The first stage in odor analysis was to flush a fresh air to the sensor array for obtain a baseline. The air response was recorded and stored in excel file for baseline correction. First stage of pre-processing consists of manipulating the sensor response with respect to its baseline (e.g., response to a reference analyte or air) for the purposes of drift compensation, contrast enhancement and scaling.

The fruit sample was placed in an airtight plastic jar called as concentration chamber having volume of 1L and it was equilibrated for 0.5hr. After 0.5hr the headspace reached a steady state and experiments were conducted. The headspace gas was pumped by using centrifugal air pump with air flow-rate 3.2 L/min through a rubber tube and non-return solenoid valves into air tight gas measurement chamber of 0.6 L capacity. The gas reaches over the MOS sensor array placed inside measurement chamber; connected to the signal conditioning unit outside the chamber as shown in fig.1. Airflow always kept constant throughout the measurement for 30 second. Then measurement chamber was locked using solenoid valves and remain steady for 60 second for reaching sensors to its steady state. The electronic valves were controlled by a LabVIEW program, guide the air and headspace as per requirement.

When the sensors exposed by the odorant gas, it produces a transient response as the VOCs interact with the surface and bulk of the sensor's active material. A steady state condition is reached in a few seconds to a few minutes, depending on the sensor type. The odor from guava fruit sample was measured by sensor array for 100 s, the collected data interval was 1 s.

The measurement process is automatically controlled by software that we developed using LabVIEW2012. Samples of each guava fruit cultivar measured twice as per experimental design. Stored data was used for pre-processing to evaluate the sensor array response. Then the sensor housing chamber flushed out for few seconds using vacuum pump suction, so as to remove the odorant mixture from the surface and bulk of the sensor's active

material [9]. The main purpose is to clean the chamber, circuits and return sensors to their baseline. By guiding air flow through electronic valves clean air enters the circuit, crosses the measurement chamber first and sucks the remaining volatiles out of the circuit using vacuum pump. The empty concentration chamber was also cleaned using this process. E-nose was operated at the temperature of 24^0 C and 40–45% RH during all experiments. The stored data is in the form of matrix array that contains 8 columns related to eight MOS sensors present in the sensor array and no. of rows related to no. of data points. This data was stored in Excel sheet format, which was used for statistical as well as neural network analysis using LabVIEW2012 and Matlab10a software. Figure 5 shows photograph of developed e-nose system and software.

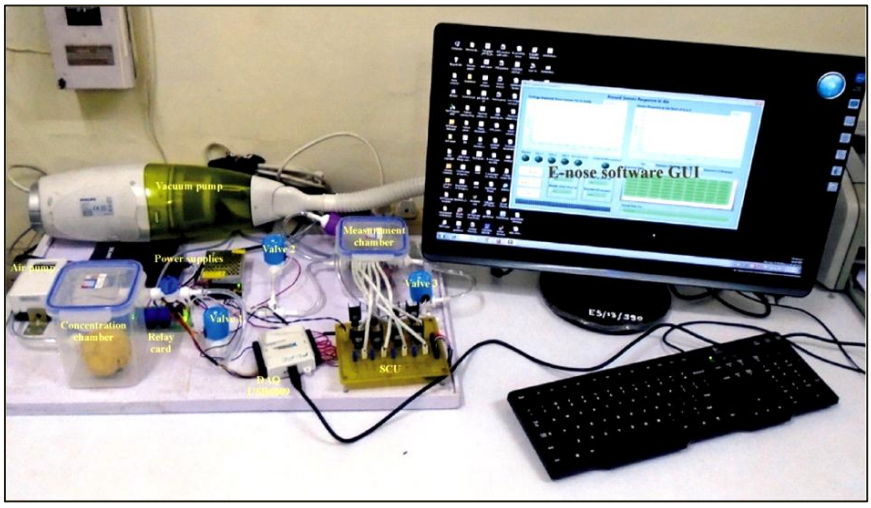

Figure 5: Developed e-nose system photograph

3. Result and Discussion:

The e-nose data was analyzed using radar plot technique shown in fig.6. The different odor signature for distinct class of ripeness was observed from the analysis. The magnitude of each axis indicates the relative response of individual sensor to the fruit odor. A unique odor-print was obtained for four ripening states of guava fruit as green, ripe, overripe and spoiled. This indicates the use of non-specific selective gas sensor arrays to construct an odor database.

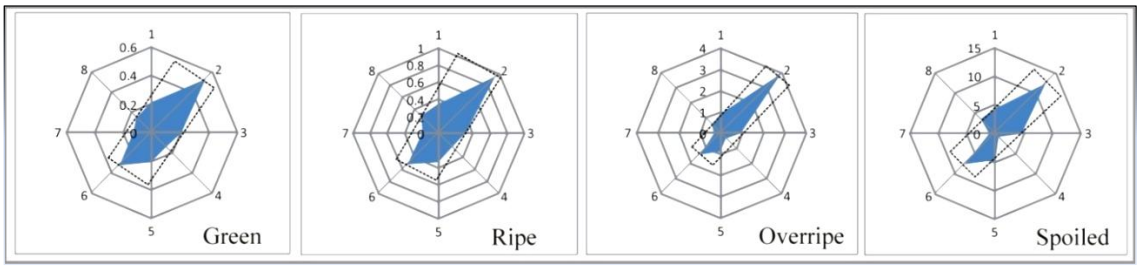

Figure 6: Radar plots explaining the discriminating power of developed e-nose for green, ripe, overripe and spoiled class of guava fruits.

The relative response of eight gas sensors were analyzed using PCA and the first two principle components are plotted in fig.7. The discrimination ability of e-nose was tested using PCA analysis. PCA analysis was applied to 400x8 data samples (100x8 data points of

each class). The two principal components $\{PC_{1,n}, PC_{2,n}\}$ was obtained and has the two greatest variances: 80.22% and 17.59% (or total cumulative variance of 97. 81%) of the variance in the input variables, respectively. The scores of the four groups of fruits was plotted for principal component 2 (PC2) versus principal component 1 (PC1). The discrimination between the four ripening states of guava as green, ripe, overripe and spoiled can be clearly seen from the figure. The processed data show a shift of the different ripening states which coinciding with the classification by trained human graders. The four clusters from left to right indicate the discrimination of fruit classes from green to spoil. A strong pattern separation was found between the four ripening classes of guava. This agrees well with human expert grading results.

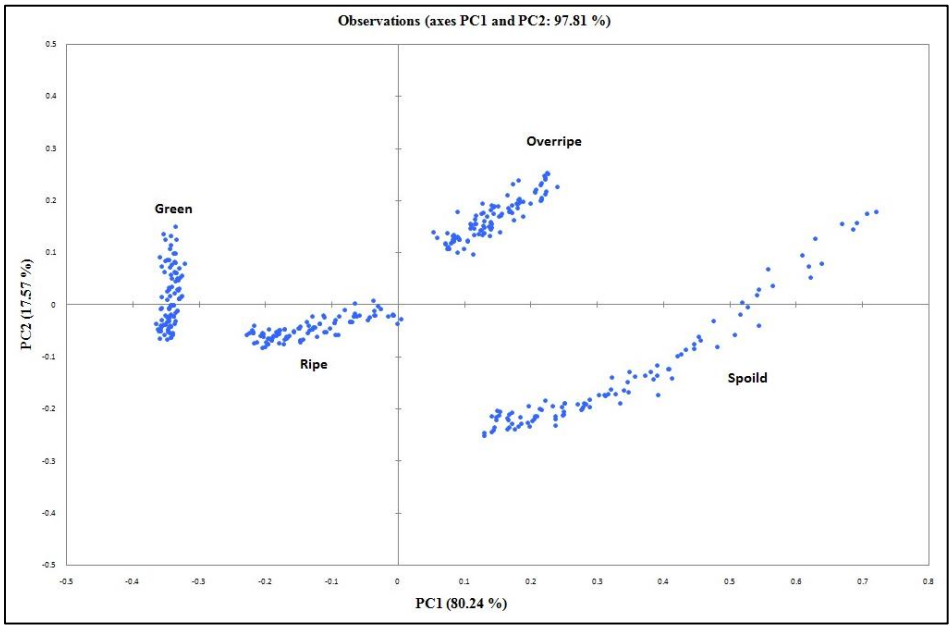

Figure 7 Two dimensional PCA plot for the response of sensor array to four ripening classes of guava fruit

The developed system has enough resolution to explain the different ripeness states. Principal components score plot proves the capability of sensor array used in e-nose with significant performance for classification of guava fruits on the basis of their ripening state. It is clearly that e-nose system that we developed, confirming well performance in classification of guava cultivar. The PCA result also showed that the four classes were appropriately separated with high pattern separation in the feature space indicates robustness of this classification system could be confirmed.

4. Conclusion

We have shown that the developed application specific e-nose system is able to classify guava fruit cultivar with high accuracy. The odours of the different ripening state guava cultivar were evaluated using developed e-nose system and were sorted into the same four classes as they were sorted by the human expert; Thus the developed e-nose is effective in discriminating various ripening classes of guava fruits. Thus developed e-nose system may be useful, simple, fast and low-cost method for classification of guava fruits.

In experiment radar plot and PCA based classification successful in separating the fruit samples into four different groups or clusters with adequate accuracy and resolution. The indigenously designed dynamic headspace sampling technique in e-nose proven to be very

useful; signals are stronger because of fruit vapors accumulated long period of time. The results obtained using our developed e-nose determines different ripening state of guava fruit successfully.

References:

[1] L. R. Verma, Dr. V. K. Joshi, "Postharvest Technology of Fruits and Vegetables: Handling, Processing, Fermentation, and Waste Management, Volume 2", Indus publishing company, 2000

[2] Kea-Tiong Tang , Shih-Wen Chiu, Chih-Heng Pan, Hung-Yi Hsieh, Yao-Sheng Liang and su-Chieh Liu,"Development of a Portable Electronic Nose System for the Detection and Classification of Fruity Odors", Sensors 2010, 10, 9179-9193; doi:10.3390/s101009179

[3] Ashok Kanade and Dr. A. D. Shaligram, "Development of an e-Nose using metal oxide semiconductor sensors for the classification of climacteric fruits", International Journal of Scientific & Engineering Research, Volume 5, Issue 2, February-2014,ISSN 2229-5518.

[4] Rashida E. El Bulk, El Fadil E. Babiker & Abdullahi H. El Tinay, "Changes in chemical composition of guava fruits during development and ripening", Food Chemistry, Vol. 59, No. 3, pp. 395-399, 1997

[5] J. Brezmes, E. Llobet, X. Vilanova, G. Saiz, X. Correig , "Fruit ripeness monitoring using an Electronic Nose", Sensors and Actuators B ,69 (2000) 223–229

[6] Gomez, A. H., Wang, J., Hu, G., & Pereira, A. G. (2006). Electronic nose technique potential monitoring mandarin maturity. Sensors and Actuators B: Chemical, 113(1), 347-353.

[7] C. Di Natale , A. Macagnano , F. Davide , A. D'Amico , R. Paolesse ,T. Boschi , M. Faccio , G. Ferri , "An electronic nose for food analysis", Sensors and Actuators B 44 (1997) 521–526

Paper 40

TOPOLOGICAL INDICES OF 2-DEOXY–D-GLUCOSE FOR COVID-19

R S Indumathi [1, a)], M R Rajesh Kanna [2, b)], H. L. Parashivamurthy [3, c)], Manjula C Gudgeri[4, d)] , Niranjan K M C[5, e)]

[1,] *Department of Mathematics, MIT Mysore, Belwadi INDIA.*
[2,] *Department of Mathematics, Sri D D Urs Government First Grade College, Hunsur INDIA.*
[3,]*Department of Mathematics, BGS Institute of technology, Adichunchangiri university, Nagamangala taluk B G nagar Mandya district, INDIA.,*

[4,]*Department of Mathematics, KLE's Dr. MSSCET, Belagavi, INDIA.*
[5,] *Department of Mathematics, UBDTCE, Davangere, INDIA.*

Abstract. : Chemists can employ graph theory to create a number of useful tools, such as "topological indices". A topological index is a numerical representation of the topological structure of Top(H) = Top(G) for every graph H that is isomorphic to G is a number belonging to a graph G. In this manuscript, we determine some indices, ABC4, ABC, Randic connectivity, GA, Sum connectivity, GA5, First, Second, First Multiple, Second Multiple, Augmented,and Hyper Zagreb indices, Harmonic, Forgotten topological, Symmetric division and also First, Second, Third Zagreb polynomials, Sombor index, Reduced Sombor index and Banhatti index of 2 Deoxy D Glucose.

INTRODUCTION

Qualitative predictions about reactivity of various compounds and the structure may obtained by chemists using simple rules provided by Graph theory. All the aspects of the application of graph theory to chemistry is concerned with chemical graph theory, which is a branch of mathematical chemistry. A molecular graph is a connected graph with atoms and chemical bonds as vertices and edges.

The medication 2-Deoxy-D-Glucose has been widely investigated in the past for the treatment of cancer as well as COVID19. The medicine is packaged as a powder in a sachet that is dissolved in water and administered orally. It builds up in virus-infected cells and prevents virus development by stopping viral synthesis and energy production.

The structures of chemical compounds are described by molecular descriptors which are nothing but topological indices. They help us to forecast certain physical and chemical properties like enthalpy of vaporization , stability, boiling point, etc. In this article, we have considered connected molecular graphs which have no multiple edges and loops.

Let G(V, E) be a graph with d_u as the degree of the vertex u. uv is an edge connected by the vertices u and v. In the paper [7] Sridhar and his co-authors determined few topological indices of Graphene.
"One of the most used topological indices with high correlation with many physical and chemical indices of molecular compounds is the Wiener index" which was studied in[10].

"The ABC index is one of the degree-based molecular descriptors", which was found by Estrada et al. [6] It may also be used to model the thermodynamic properties of organic molecules as well as the stability of branched alkanes.

Definition1.1. "ABC index" of G is stated as,

$$\mathrm{ABC(G)} = \sum_{e=uv\in E(G)} \sqrt{\frac{d_u + d_v - 2}{d_u d_v}}$$

The GA index was established by D. Vukicevic et.al. Have a look on further additional information [1, 5]

Definition 1.2. GA index can be stated as

$$GA(G) = \sum_{e=uv\in E(G)} \frac{2\sqrt{d_u d_v}}{d_u+d_v}.$$

Definition 1.3. *Zhou and Trinajstic* established a Sum connectivity index index as,

$$S(G) = \sum_{e=uv\in E(G)} \frac{1}{\sqrt{d_u+d_v}}$$

Definition1.4. One of the oldest topological indices based on degrees. which contributes quantitative measurement of branching of molecules is Randic index and is defined as.

$$R(G) = \sum_{e=uv\in E(G)} \frac{1}{\sqrt{d_u d_v}}$$

Definition 1.5. Zhong established Harmonic index can be stated as below

$$H(G) = \sum_{e=uv\in E(G)} \left(\frac{2}{d_u+d_v}\right)$$

Definition 1.6. G. H. Shirdel et.al[12] established Hyper-Zagreb index can be stated as

$$HM(G) = \sum_{e=uv\in E(G)} (d_u+d_v)^2$$

For scientists in the pharmaceutical and medical fields, the forgotten topological index has proven to be valuable. It was used for building the biological and molecular characteristics of the most recent medications. Such tactics are widely used in developing countries where there is a shortage of money for the purchase of relevant chemical reagents and equipment.

Definition 1.7. "***F***urtula and ***G***utman" (2015) [3] established the forgotten topological index (also known as the F-index), which is defined as

$$F(G) = \sum_{e=uv\in E(G)} ({d_u}^2 + {d_v}^2)$$

Definition 1.8. Furtula et al [4]established **A**ugmented Zagreb index as

$$AZI(G) = \sum_{e=uv\in E(G)} \left(\frac{d_u d_v}{d_u+d_v-2}\right)^3$$

Definition 1.9. First and second Zagreb indices can be stated as

$$M_1(G) = \sum_{e=uv\in E(G)} (d_u+d_v)$$

$$M_2(G) = \sum_{e=uv\in E(G)} (d_u d_v)$$

Definition 2.0. "Fourth atom bond connectivity index" was established by M. Ghorbani et al. [11] in 2010 and it is stated as

$$ABC_4(\mathrm{G}) = \sum_{e=uv\in E(G)} \sqrt{\frac{S_u+S_v-2}{S_u S_v}}$$

where S_u indicates sum of the degrees of all neighbours of vertex u in G, similarly for S_v

Definition 2.1. The "Fifth Geometric-arithmetic index", was found by A.Graovac et al [1] in 2011, and is stated as

$GA_5(G) = \sum_{uv\in E} \frac{2\sqrt{S_u+S_v}}{S_u+S_v}$.

Definition 2.2 "Multiple Zagreb topological indices" of a graph G, based on the degree of vertices of G, were developed by M. Ghorbani and N. Azimi [8] in 2012. The following are the definitions for the first and second multiple Zagreb indices:

$PM_1(G) = \prod_{e=uv\in E}(d_u + d_v)$, $PM_2(G) = \prod_{e=uv\in E}(d_u d_v)$

Definition 2.3. The "First, Second, and Third Zagreb Polynomials" were introduced by Faith-Tabar [2] in 2011.

$$ZG_1(G) = \sum_{e=uv\in E} x^{d_u+d_v}$$

$$ZG_2(G) = \sum_{e=uv\in E} x^{d_u d_v}$$

$$ZG_3(G) = \sum_{e=uv\in E} x^{|d_u-d_v|}$$

Definition 2. 4. Some new degree-based graph invariants have been discovered, and they play an essential role in chemical graph theory. These topological indices can be used to calculate total surface area and heat formation in chemical compounds. The invariants of these graphs are as follows: Index of symmetric division

$$SDD(G) = \sum_{e=uv\in E}\left\{\frac{min(d_u,d_v)}{max(d_u,d_v)} + \frac{max\,(d_u,d_v)}{min(d_u,d_v)}\right\}$$

Definition 2. 5. A novel graph invariant called the Sombor index of a graph is introduced by Gutman et.al [9] and it is stated as
$SO(G) = \sum_{uv\in E}(\sqrt{d_u^2 + d_v^2})$.

Definition 2. 6. Recently I. Gutman established Reduced Sombor Index and it is stated as $SO_{red}(G) = \sum_{uv\in E}\left(\sqrt{(d_u - 1)^2 + (d_v - 1)^2}\right)$, where d_u represents the degree of the vertex u, similarly for d_v.

It was shown that the reduced Sombor index can help to exhibit small discriminative potential and forecast physico-chemical properties of molecules, and that it performs slightly better than the Sombor index in this regard. Based on the results of a test of decreased Sombor indices' predictive potential, it has been successfully applied to "modelling thermodynamic properties of substances."

Definition 2. 7. **"**Banhatti sombor index" of a connected graph G was established by Kulli [14] and is stated as

$$BSO(G) = \sum_{uv\in E(G)}\sqrt{\left(\frac{1}{{d_u}^2} + \frac{1}{{d_v}^2}\right)}$$

MAIN RESULTS

Theorem 2 1. The "Atom bond connectivity index" of 2 Deoxy D Glucose For Covid-19 is 7 .98502365.

Proof. Consider a 2-Deoxy-D- Glucose $C_6H_{12}O_5$. Let $m_{i,j}$be the edges that connect the vertices of degrees $d_i$and d_j. "Two-dimensional structure of 2-Deoxy- D- Glucose" (as depicted in Figure-1) contains edges of the type $m_{1,3}$, $m_{2,2}$, $m_{2,3}$ and $m_{3,3}$. The number edges of these types, as shown in the diagram, are as follows: $|m_{1,2}|$=1, $|m_{1,3}|$=3, $|m_{2,2}|$=1, $|m_{2,3}|$=3 and $|m_{3,3}|$=3

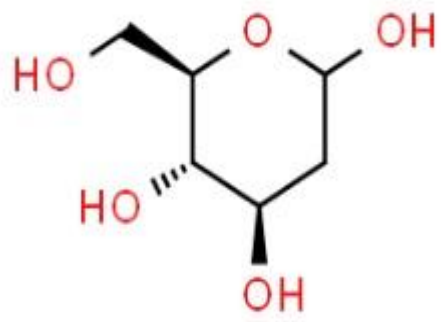

Figure 1: 2-Deoxy-D-glucose - $C_6H_{12}O_5$

"Atom bond connectivity index" of 2 Deoxy D Glucose

$$\mathrm{ABC}(C_6H_{12}O_5) = \sum_{e=uv\in E(G)} \sqrt{\frac{d_u + d_v - 2}{d_u d_v}}$$

$$= |\boldsymbol{m_{1,2}}| \left(\sqrt{\frac{1+2-2}{1.2}}\right) + |\boldsymbol{m_{1,3}}| \left(\sqrt{\frac{1+3-2}{1.3}}\right) + |\boldsymbol{m_{2,2}}| \left(\sqrt{\frac{2+2-2}{2.2}}\right) + |\boldsymbol{m_{2,3}}| \left(\sqrt{\frac{2+3-2}{2.3}}\right) + |\boldsymbol{m_{3,3}}| \left(\sqrt{\frac{3+3-2}{3.3}}\right).$$

$$= (1)\left(\frac{\mathbf{1}}{\sqrt{\mathbf{2}}}\right) + (3)\left(\sqrt{\frac{2}{3}}\right) + (1)\left(\frac{\mathbf{1}}{\sqrt{\mathbf{2}}}\right) + (3)\left(\frac{1}{\sqrt{2}}\right) + (3)\left(\frac{\mathbf{2}}{\mathbf{3}}\right).$$

$\therefore \boldsymbol{ABC(G)} = 7.98502365.$

Theorem 2.2 The "Fourth atom bond connectivity index" of 2- Deoxy- D -Glucose is 6 . 28152996.

Proof. Let $e_{i,j}$ denotes the edges of 2- Deoxy -D -Glucose with i = S_u and j =S_v. The summation of degrees of edge endpoints of 2- Deoxy- D- Glucose has six edge kinds, as can be seen. $e_{2,2}$, $e_{2,4}$, $e_{3,6}$, $e_{3,7}$, $e_{4,7}$,$e_{5,5}$, $e_{5,6}$,$e_{5,7}$, $e_{6,7}$ and $e_{7,7}$ as depicted in figure 2. Clearly from the figure 1,

$$|e_{2,4}| = 1, |e_{3,6}| = 1, |e_{3,7}| = 2, |e_{4,7}| = 1, |e_{5,5}| = 1, |e_{5,6}| = 1, |e_{5,7}| = 1, |e_{6,7}| = 1 \; and \; |e_{7,7}| = 2$$

The ABC_4 index of 2 Deoxy D Glucose

$$\mathrm{ABC}_4(C_6H_{12}O_5) = \sum_{e=uv\in E(G)} \sqrt{\frac{S_u + S_v - 2}{S_u S_v}}$$

$$= |e_{2,4}| \left(\sqrt{\frac{2+4-2}{2.4}}\right) + |e_{3,6}| \left(\sqrt{\frac{3+6-2}{3.6}}\right) + |e_{3,7}| \left(\sqrt{\frac{3+7-2}{3.7}}\right) + |e_{4,7}| \left(\sqrt{\frac{4+7-2}{4.7}}\right) +$$

$$|e_{5,5}| \left(\sqrt{\frac{4+5-2}{5.5}}\right) + |e_{5,6}| \left(\sqrt{\frac{5+6-2}{5.6}}\right) + |e_{5,7}| \left(\sqrt{\frac{5+7-2}{5.7}}\right) + |e_{6,7}| \left(\sqrt{\frac{6+7-2}{6.7}}\right) + |e_{7,7}| \left(\sqrt{\frac{7+7-2}{7.7}}\right).$$

$$= 1\left(\sqrt{\frac{4}{8}}\right) + 1\left(\sqrt{\frac{7}{18}}\right) + 2\left(\sqrt{\frac{8}{21}}\right) + 1\left(\sqrt{\frac{9}{28}}\right) + 1\left(\sqrt{\frac{8}{25}}\right) + 1\left(\sqrt{\frac{9}{30}}\right) + 1\left(\sqrt{\frac{10}{35}}\right) + 1\left(\sqrt{\frac{11}{42}}\right) + 2\left(\sqrt{\frac{12}{49}}\right)$$

$$= 6.28152996$$

Theorem 2.3 The Randic connectivity index of 2 -Deoxy -D –Glucose for Covid-19 is 5. 16390246.

Proof. TheRandic connectivity index of 2- Deoxy- D- Glucose is

$$\vartheta(C_6H_{12}O_5) = \sum_{e=uv\in E(G)} \frac{1}{\sqrt{d_u d_v}}$$

$$= |\boldsymbol{m_{1,2}}| \left(\tfrac{1}{\sqrt{1.2}}\right) + |\boldsymbol{m_{1,3}}|\left(\tfrac{1}{\sqrt{1.3}}\right) + |\boldsymbol{m_{2,2}}|\left(\tfrac{1}{\sqrt{2.2}}\right) + |\boldsymbol{m_{2,3}}|\left(\tfrac{1}{\sqrt{2.3}}\right) + |\boldsymbol{m_{3,3}}|\left(\tfrac{1}{\sqrt{3.3}}\right).$$

$$= 1\left(\frac{1}{\sqrt{2}}\right) + 3\left(\frac{1}{\sqrt{3}}\right) + 1\left(\frac{1}{\sqrt{4}}\right) + 3\left(\frac{1}{\sqrt{6}}\right) + 3\left(\frac{1}{3}\right)$$

$\therefore \vartheta(C_6H_{12}O_5) = 5.16390246.$

Theorem 2 4 The Sum connectivity index of 2 -Deoxy -D –Glucose for Covid-19 is 5. 14373.

Proof. The Sum connectivity index of 2- Deoxy- D- Glucose is

$$\mathrm{S}(C_6H_{12}O_5) = \sum_{e=uv\in E(G)} \frac{1}{\sqrt{d_{u+} d_v}}$$

$$= |\boldsymbol{m_{1,2}}| \left(\tfrac{1}{\sqrt{1+2}}\right) + |\boldsymbol{m_{1,3}}|\left(\tfrac{1}{\sqrt{1+3}}\right) + |\boldsymbol{m_{2,2}}|\left(\tfrac{1}{\sqrt{2+2}}\right) + |\boldsymbol{m_{2,3}}|\left(\tfrac{1}{\sqrt{2+3}}\right) + |\boldsymbol{m_{3,3}}|\left(\tfrac{1}{\sqrt{3+3}}\right).$$

$$= 1\left(\frac{1}{\sqrt{3}}\right) + 3\left(\frac{1}{\sqrt{4}}\right) + 1\left(\frac{1}{\sqrt{4}}\right) + 3\left(\frac{1}{\sqrt{5}}\right) + 3\left(\frac{1}{6}\right)$$

$\therefore \mathrm{S}(C_6H_{12}O_5) = 5.14373.$

Theorem 2 5 The GA index of 2 -Deoxy -D –Glucose for Covid-19 is 10. 48027.

Proof. The GA index of 2- Deoxy- D- Glucose is

$$\mathrm{GA}(C_6H_{12}O_5) = \sum_{e=uv\in E(G)} \frac{2\sqrt{d_u d_v}}{d_u + d_v}$$

$$= |\boldsymbol{m_{1,2}}| \left(\tfrac{2\sqrt{1.2}}{1+2}\right) + |\boldsymbol{m_{1,3}}|\left(\tfrac{2\sqrt{1.3}}{1+3}\right) + |\boldsymbol{m_{2,2}}|\left(\tfrac{2\sqrt{2.2}}{2+2}\right) + |\boldsymbol{m_{2,3}}|\left(\tfrac{2\sqrt{2.3}}{2+3}\right) + |\boldsymbol{m_{3,3}}|\left(\tfrac{2\sqrt{3.3}}{3+3}\right).$$

$$= 1\left(\frac{2\sqrt{2}}{3}\right) + 3\left(\frac{2\sqrt{3}}{4}\right) + 1\left(\frac{4}{4}\right) + 3\left(\frac{2\sqrt{6}}{5}\right) + 3\left(\frac{6}{6}\right)$$

$\therefore \mathrm{S}(C_6H_{12}O_5) = 10.48027.$

Theorem 2 6 The fifth GA index of 2 -Deoxy -D –Glucose for Covid-19 is 11 .6596943.

Proof. The fifth GA index of 2- Deoxy- D- Glucose is

$$\mathrm{GA}_5(C_6H_{12}O_5) = \sum_{e=uv\in E(G)} \frac{2\sqrt{S_u S_v}}{S_u + S_v}$$

$$= \left|e_{2,4}\right| \left(\tfrac{2\sqrt{2.4}}{2+4}\right) + \left|e_{3,6}\right| \left(\tfrac{2\sqrt{3.6}}{3+6}\right) + \left|e_{3,7}\right| \left(\tfrac{2\sqrt{3.7}}{3+7}\right) + \left|e_{4,7}\right| \left(\tfrac{2\sqrt{4.7}}{4+7}\right) + \left|e_{5,5}\right| \left(\tfrac{2\sqrt{5.5}}{5+5}\right) + \left|e_{5,6}\right| \left(\tfrac{2\sqrt{5.6}}{5+6}\right) + \left|e_{5,7}\right| \left(\tfrac{2\sqrt{5.7}}{5+7}\right) + \left|e_{6,7}\right| \left(\tfrac{2\sqrt{6.7}}{6+7}\right) + \left|e_{7,7}\right| \left(\tfrac{2\sqrt{7.7}}{7+7}\right).$$

$$= 1\left(\frac{2\sqrt{8}}{6}\right) + 1\left(\frac{2\sqrt{18}}{9}\right) + 2\left(\frac{2\sqrt{21}}{10}\right) + 1\left(\frac{2\sqrt{28}}{11}\right) + 1\left(\frac{2\sqrt{25}}{10}\right) + 1\left(\frac{2\sqrt{30}}{11}\right) + 1\left(\frac{2\sqrt{35}}{12}\right) + 1\left(\frac{2\sqrt{42}}{13}\right) + 2\left(\frac{2\sqrt{49}}{14}\right)$$

∴ $\mathrm{GA}_5(C_6H_{12}O_5)$= 11 .6596943.

Theorem 2.7. The First Zagreb index of 2 -Deoxy -D –Glucose for Covid-19 is 52.

Proof. The First Zagreb index of 2- Deoxy- D- Glucose is

$$\mathrm{M}_1(C_6H_{12}O_5) = \sum_{e=uv\in E(G)} (d_u + d_v)$$

$$= |\boldsymbol{m_{1,2}}|\,(1+2) + |\boldsymbol{m_{1,3}}|(1+3) + |\boldsymbol{m_{2,2}}|(2+2) + |\boldsymbol{m_{2,3}}|(2+3) + |\boldsymbol{m_{3,3}}|(3+3).$$

$$= 1(3) + 3(4) + 1(4) + 3(5) + 3(6)$$

∴ $\mathrm{M}_1(C_6H_{12}O_5)$= 52

Theorem 2.8. The "Second Zagreb index" of 2 -Deoxy -D –Glucose for Covid-19 is 60.

Proof. The Second Zagreb index of 2- Deoxy- D- Glucose is

$$\mathrm{M}_1(C_6H_{12}O_5) = \sum_{e=uv\in E(G)} (d_u d_v)$$

$$= |\boldsymbol{m_{1,2}}|\,(1.2) + |\boldsymbol{m_{1,3}}|(1.3) + |\boldsymbol{m_{2,2}}|(2.2) + |\boldsymbol{m_{2,3}}|(2.3) + |\boldsymbol{m_{3,3}}|(3.3).$$

$$= 1(2) + 3(3) + 1(4) + 3(65) + 3(9)$$

∴ $\mathrm{M}_1(C_6H_{12}O_5)$= 60

Theorem 2.9. The "First multiple Zagreb index" of 2 -Deoxy -D –Glucose for Covid-19 is 2.0736X10^7.

Proof. The First multiple Zagreb index of 2- Deoxy- D- Glucose is

$$\mathrm{PM}_1(C_6H_{12}O_5) = \prod_{e=uv\in E(G)} (d_u + d_v)$$

$$= \prod_{e=uv\in \boldsymbol{m_{1,2}}}(d_u + d_v).\ \prod_{e=uv\in \boldsymbol{m_{1,3}}}(d_u + d_v).\ \prod_{e=uv\in \boldsymbol{m_{2,2}}}(d_u + d_v).$$

$$\prod_{e=uv\in \boldsymbol{m_{2,3}}}(d_u + d_v).\ \prod_{e=uv\in \boldsymbol{m_{3,3}}}(d_u + d_v).$$

$$= 3^1 \times 4^3 \times 4^1 \times 5^3 \times 6^3$$

∴ $\mathrm{PM}_1(C_6H_{12}O_5)$= 2.0736X$10^7$

Theorem 3.0. The "Second multiple Zagreb index" of 2 -Deoxy -D –Glucose for Covid-19 is 3.4012224X10^7.

Proof. The "Second multiple Zagreb" index of 2- Deoxy- D- Glucose is

$$\mathrm{PM}_2(C_6H_{12}O_5) = \prod_{e=uv\in E(G)} (d_u d_v)$$

$$= \prod_{e=uv\in \boldsymbol{m_{1,2}}}(d_u d_v).\ \prod_{e=uv\in \boldsymbol{m_{1,3}}}(d_u d_v).\ \prod_{e=uv\in \boldsymbol{m_{2,2}}}(d_u d_v).$$

$\prod_{e=uv\in m_{2,3}}(d_u d_v).\ \prod_{e=uv\in m_{3,3}}(d_u d_v).$

$= 2^1 \times 3^3 \times 4^1 \times 6^3 \times 9^3$

$\therefore \mathrm{PM}_1(C_6H_{12}O_5) = 3.4012224\mathrm{X}10^7.$

Theorem 3.1 The Augmented Zagreb index of 2 -Deoxy -D –Glucose for Covid-19 is 84.2968.

Proof. The Augmented Zagreb index of 2- Deoxy- D- Glucose is

$$\mathrm{AZI}(C_6H_{12}O_5) = \sum_{e=uv\in E(G)} \left[\frac{d_u d_v}{d_u + d_v - 2}\right]^3$$

$$= |\boldsymbol{m_{1,2}}|\left[\frac{1.2}{1+2-2}\right]^3 + |\boldsymbol{m_{1,3}}|\left[\frac{1.3}{1+3-2}\right]^3 + |\boldsymbol{m_{2,2}}|\left[\frac{2.2}{2+2-2}\right]^3 + |\boldsymbol{m_{2,3}}|\left[\frac{2.3}{2+3-2}\right]^3 + |\boldsymbol{m_{3,3}}|\left[\frac{3.3}{3+3-2}\right]^3.$$

$$= 1\left[\frac{2}{1}\right]^3 + 3\left[\frac{3}{2}\right]^3 + 1\left[\frac{4}{2}\right]^3 + 3\left[\frac{6}{3}\right]^3 + 3\left[\frac{9}{4}\right]^3$$

$\therefore \vartheta(C_6H_{12}O_5) = 84.2968.$

Theorem 3.2 The Harmonic index of 2 -Deoxy -D –Glucose for Covid-19 is 4 . 866666666.

Proof. The "Harmonic index" of 2- Deoxy- D- Glucose is

$$\mathrm{H}(C_6H_{12}O_5) = \sum_{e=uv\in E(G)} \frac{2}{d_u + d_v}$$

$$= |\boldsymbol{m_{1,2}}|\left(\frac{2}{1+2}\right) + |\boldsymbol{m_{1,3}}|\left(\frac{2}{1+3}\right) + |\boldsymbol{m_{2,2}}|\left(\frac{2}{2+2}\right) + |\boldsymbol{m_{2,3}}|\left(\frac{2}{2+3}\right) + |\boldsymbol{m_{3,3}}|\left(\frac{2}{3+3}\right).$$

$$= 1\left(\frac{2}{3}\right) + 3\left(\frac{2}{4}\right) + 1\left(\frac{2}{4}\right) + 3\left(\frac{2}{5}\right) + 3\left(\frac{2}{6}\right)$$

$\therefore \mathrm{H}(C_6H_{12}O_5) = 4 . 866666666.$

Theorem 3.3 The Hyper Zagreb index of 2 -Deoxy -D –Glucose for Covid-19 is 256.

Proof. The Hyper Zagreb of 2- Deoxy- D- Glucose is

$$\mathrm{HM}(C_6H_{12}O_5) = \sum_{e=uv\in E(G)} (d_u + d_v)^2$$

$$= |\boldsymbol{m_{1,2}}|\,(1+2)^2 + |\boldsymbol{m_{1,3}}|(1+3)^2 + |\boldsymbol{m_{2,2}}|(2+2)^2 + |\boldsymbol{m_{2,3}}|(2+3)^2 + |\boldsymbol{m_{3,3}}|(3+3)^2$$

$$= 1(3)^2 + 3(4)^2 + 1(4)^2 + 3(5)^2 + 3(6)^2$$

$\therefore \mathrm{HM}(C_6H_{12}O_5) = 256.$

Theorem 3.4 The First Zagreb polynomial of 2 -Deoxy -D –Glucose for Covid-19 is $3x^6 + 3x^5 + 4x^4 + x^3$.

Proof. The First Zagreb polynomial of 2- Deoxy- D- Glucose is

$$\mathrm{ZG}_1(C_6H_{12}O_5) = \sum_{e=uv\in E(G)} \mathrm{x}^{d_u + d_v}$$

$= |\boldsymbol{m_{1,2}}| \mathrm{X}^{1+2} + |\boldsymbol{m_{1,3}}|\mathrm{X}^{1+3} + |\boldsymbol{m_{2,2}}|\mathrm{X}^{2+2} + |\boldsymbol{m_{2,3}}|\mathrm{X}^{2+3} + |\boldsymbol{m_{3,3}}|\mathrm{X}^{3+3}$

$= 1(\mathrm{X})^3 + 3(\mathrm{X})^4 + 1(4)^4 + 3(\mathrm{X})^5 + 3(\mathrm{X})^6$

$\therefore \mathrm{ZG}_1(C_6H_{12}O_5) = x^6 + 3x^5 + 4x^4 + x^3.$

Theorem 3.5 The Second Zagreb polynomial of 2 -Deoxy -D –Glucose for Covid-19 is $3x^9 + 3x^6 + x^4 + 3x^3 + x^2$.

Proof. The Second Zagreb polynomial of 2- Deoxy- D- Glucose is

$$\mathrm{ZG}_2(C_6H_{12}O_5) = \sum_{e=uv\in E(G)} \mathrm{X}^{d_u d_v}$$

$= |\boldsymbol{m_{1,2}}| \mathrm{X}^{1\times 2} + |\boldsymbol{m_{1,3}}|\mathrm{X}^{1\times 3} + |\boldsymbol{m_{2,2}}|\mathrm{X}^{2\times 2} + |\boldsymbol{m_{2,3}}|\mathrm{X}^{2\times 3} + |\boldsymbol{m_{3,3}}|\mathrm{X}^{3\times 3}$

$= 1(\mathrm{X})^2 + 3(\mathrm{X})^3 + 1(\mathrm{X})^4 + 3(\mathrm{X})^6 + 3(\mathrm{X})^9$

$\therefore \mathrm{ZG}_2(C_6H_{12}O_5) = 3x^9 + 3x^6 + x^4 + 3x^3 + x^2.$

Theorem 3.6 The Third Zagreb polynomial of 2 -Deoxy -D –Glucose for Covid-19 is $3x^2 + 4x + 4$.

Proof. The Third Zagreb polynomial of 2- Deoxy- D- Glucose is

$$\mathrm{ZG}_3(C_6H_{12}O_5) = \sum_{e=uv\in E(G)} \mathrm{X}^{|d_u - d_v|}$$

$= |\boldsymbol{m_{1,2}}| \mathrm{X}^{|1-2|} + |\boldsymbol{m_{1,3}}|\mathrm{X}^{|1-3|} + |\boldsymbol{m_{2,2}}|\mathrm{X}^{|2-2|} + |\boldsymbol{m_{2,3}}|\mathrm{X}^{|2-3|} + |\boldsymbol{m_{3,3}}|\mathrm{X}^{|3-3|}$

$= 1(\mathrm{X})^1 + 3(\mathrm{X})^2 + 1(\mathrm{X})^0 + 3(\mathrm{X})^1 + 3(\mathrm{X})^0$

$\therefore \mathrm{ZG}_3(C_6H_{12}O_5) = 3x^2 + 4x + 4.$

Theorem 3.7 The Forgotten topological index of 2 -Deoxy -D –Glucose for Covid-19 is 136.

Proof. The Forgotten topological index of 2- Deoxy- D- Glucose is

$$\mathrm{F}(C_6H_{12}O_5) = \sum_{e=uv\in E(G)} (\mathrm{d_u}^2 + \mathrm{d_v}^2)$$

$= |\boldsymbol{m_{1,2}}| (1^2 + 2^2) + |\boldsymbol{m_{1,3}}|(1^2 + 3^2) + |\boldsymbol{m_{2,2}}|(2^2 + 2^2) + |\boldsymbol{m_{2,3}}|(2^2 + 3^2) + |\boldsymbol{m_{3,3}}|(3^2 + 3^2)$

$= 1 \times 5 + 3 \times 10 + 1 \times 8 + 3 \times 13 + 3 \times 18$

$\therefore \mathrm{F}(C_6H_{12}O_5) = 136.$

Theorem 3.8 The Forgotten polynomial of 2 -Deoxy -D –Glucose for Covid-19 is $3x^{18} + 3x^{13} + 3x^{10} + x^8 + x^6$.

Proof. The Forgotten polynomial of 2- Deoxy- D- Glucose is

$$\mathrm{FP}(C_6H_{12}O_5) = \sum_{e=uv\in E(G)} \mathrm{X}^{({d_u}^2 + {d_v}^2)}$$

$= |\boldsymbol{m_{1,2}}| \mathrm{X}^{(1^2+2^2)} + |\boldsymbol{m_{1,3}}|\mathrm{X}^{(1^2+3^2)} + |\boldsymbol{m_{2,2}}|\mathrm{X}^{(2^2+2^2)} + |\boldsymbol{m_{2,3}}|\mathrm{X}^{(2^2+3^2)} + |\boldsymbol{m_{3,3}}|\mathrm{X}^{(3^2+3^2)}$

$= 1(\mathrm{X})^5 + 3(\mathrm{X})^{10} + 1(\mathrm{X})^8 + 3(\mathrm{X})^{13} + 3(\mathrm{X})^{18}$

$\therefore \mathrm{FP}(C_6H_{12}O_5) = 3x^{18} + 3x^{13} + 3x^{10} + x^8 + x^6.$

Theorem 3.9 The Symmetric division index of 2 -Deoxy -D –Glucose is 23.

Proof. The Symmetric division index of 2- Deoxy- D- Glucose is

$$\mathrm{SDD}(C_6H_{12}O_5) = \sum_{e=uv\in E(G)} \left\{\frac{min(d_u,d_v)}{max(d_u,d_v)} + \frac{max(d_u,d_v)}{min(d_u,d_v)}\right\}$$

$$= |\boldsymbol{m_{1,2}}| \left\{\frac{\min(1,\ 2)}{\max(1,\ 2)} + \frac{\max(1,\ 2)}{\min(1,\ 2)}\right\} + |\boldsymbol{m_{1,3}}|\left\{\frac{\min(1,\ 3)}{\max(1,\ 3)} + \frac{\max(1,\ 3)}{\min(1,\ 3)}\right\} + |\boldsymbol{m_{2,2}}|\left\{\frac{\min(2,\ 2)}{\max(2,\ 2)} + \frac{\max(2,\ 2)}{\min(2,\ 2)}\right\}$$
$$+ |\boldsymbol{m_{2,3}}|\left\{\frac{\min(2,\ 3)}{\max(2,\ 3)} + \frac{\max(2,\ 3)}{\min(2,\ 3)}\right\} + |\boldsymbol{m_{3,3}}|\left\{\frac{\min(3,\ 3)}{\max(3,\ 3)} + \frac{\max(3,\ 3)}{\min(3,\ 3)}\right\}$$

$$= 1\left(\frac{5}{2}\right) + 3\left(\frac{10}{3}\right) + 1(1) + 3\left(\frac{13}{6}\right) + 3(1)$$

$\therefore \mathrm{SDD}(C_6H_{12}O_5) = 23.$

Theorem 4.0 The Sombor index of 2 -Deoxy -D –Glucose for Covid-19 is 38.0959.

Proof. The Sombor index of 2- Deoxy- D- Glucose is

$$\mathrm{SO}(C_6H_{12}O_5) = \sum_{e=uv\in E(G)} \sqrt{\left({d_u}^2 + {d_v}^2\right)}$$

$$= |\boldsymbol{m_{1,2}}| \sqrt{\left(1^2 + 2^2\right)} + |\boldsymbol{m_{1,3}}|\sqrt{(1^2 + 3^2)} + |\boldsymbol{m_{2,2}}|\sqrt{(2^2 + 2^2)} + |\boldsymbol{m_{2,3}}|\sqrt{\left(2^2 + 3^2\right)} +$$
$$|\boldsymbol{m_{3,3}}|\sqrt{(3^2 + 3^2)}$$

$$= 1 \times \sqrt{5} + 3 \times \sqrt{10} + 1 \times \sqrt{8} + 3 \times \sqrt{13} + 3 \times \sqrt{18}$$

$\therefore \mathrm{SO}(C_6H_{12}O_5) = 38.0959.$

Theorem 4.1 The Reduced Sombor index of 2 -Deoxy -D –Glucose for Covid-19 is 23.6077.

Proof. The Reduced Sombor index of 2- Deoxy- D- Glucose is

$$SO_{red}(C_6H_{12}O_5) = \sum_{e=uv\in E(G)} \sqrt{\left((d_u - 1)^2 + (d_v - 1)^2\right)}$$

$$= |\boldsymbol{m_{1,2}}| \sqrt{\left(0^2 + 1^2\right)} + |\boldsymbol{m_{1,3}}|\sqrt{(0^2 + 2^2)} + |\boldsymbol{m_{2,2}}|\sqrt{(1^2 + 1^2)} + |\boldsymbol{m_{2,3}}|\sqrt{\left(1^2 + 2^2\right)} +$$
$$|\boldsymbol{m_{3,3}}|\sqrt{(2^2 + 2^2)}$$

$$= 1 \times \sqrt{1} + 3 \times \sqrt{4} + 1 \times \sqrt{2} + 3 \times \sqrt{5} + 3 \times \sqrt{8}$$

$\therefore \mathrm{SO_{red}}(C_6H_{12}O_5) = 23.6077.$

Theorem 4.2 The Banhatti Sombor index of 2 -Deoxy -D –Glucose for Covid-19 is 8.2044

Proof.
The Banhatti Sombor index of 2 -Deoxy -D –Glucose is

$$BSO(G) = \sum_{uv\in E(G)} \sqrt{\left(\frac{1}{{d_u}^2} + \frac{1}{{d_v}^2}\right)}$$

$$= |m_{1,2}|\sqrt{\frac{1}{1^2}+\frac{1}{2^2}} + |m_{1,3}|\sqrt{\frac{1}{1^2}+\frac{1}{3^2}} + |m_{2,2}|\sqrt{\frac{1}{2^2}+\frac{1}{2^2}} + |m_{2,3}|\sqrt{\frac{1}{2^2}+\frac{1}{3^2}} + |m_{3,3}|\sqrt{\frac{1}{3^2}+\frac{1}{3^2}}$$

.

$$= 1\times\sqrt{1+\frac{1}{4}} + 3\times\sqrt{1+\frac{1}{9}} + 1\times\sqrt{\frac{1}{4}+\frac{1}{4}} + 3\times\sqrt{\frac{1}{4}+\frac{1}{9}} + 3\times\sqrt{\frac{1}{9}+\frac{1}{9}}$$

$$\therefore BSO(G) = 8.2044.$$

CONCLUSIONS

In this article we have calculated topological indices of 2 -Deoxy -D –Glucose without using computer.

REFERENCES

1. A. Graovac, M. Ghorbani, M. A. Hosseinzadeh, Computing Fifth Geometric-Arithmetic index for nanostar dendrimers, J. Math. Nanosci. , 1, (2011) 33-42
2. Ali Astanesh-Asl and G. H Fath-Tabar, Computing the first and third Zagreb polynomials of certained product of graphs, Irsnisn Journal of Marhematical Chemistry. 2-2 (2011), 73 - 78.
3. B. Furtula and Gutman .I, A forgotton topological index, J. Math. Chem. 53 (2015) 213 - 220.
4. B. Furtula, A. Graovac, D. Vuki_cevi_c, Augmented Zagreb index, J. Math. Chem. 48 (2010) 370 -380 .
5. D. Vukicevic-B. Furtula, Topological index based on the ratios of geometrical and arithmetical means of end-vertex degrees of edges, { *J. Math. Chem.*}, {46}, (2009) 1369-1376.
6. E. Estrada, L. Torres, L. Rodriguez, I. Gutman, An atom-bond connectivity index: Modelling the enthalpy of formation of alkanes, Indian J. Chem. 37A (1998), 849-855.
7. G. Sridhara, M. R. Rajesh Kanna, and R. S. Indumathi. Computation of Topo- logical Indices of Graphene.Journal of nanomaterial Volume (2015) , Article ID 969348, 8 pages.
8. Ghorbani M, Azimi N. Note on multiple Zagreb indices. Iranian Journal of Math- ematical Chemistry. 2012; 3(2): 137-143.
9. Gutman I. Geometric approach to degree-based topological indices Sombor in- dices. MATCH Commun. Math. Comput. Chem. 2021, 86, 11-16.
10. H. Wiener, Structural determination of the Paraffinn boiling points, J. Am. Chem. Soc. 69 (1947) 17-20.
11. M. Ghorbani, M. A. Hosseinzadeh, Computing ABC4 index of Nanostar den- drimers. Optoelectron. Adv. Mater-Rapid commun. 4(9), (2010), 1419-1422.
12. Shirdel, G.H., RezaPour H., Sayadi. A.M. The Hyper-Zagreb Index of Graph Operations. { *Iranian Journal of Mathematical Chemistry*,} {4(2)}, (2013), 213-220.
13. S .Chen, W. Liu, the geometric-arithemtic index of nanotubes, *{ J. Comput. Theor. Nanosci.*} {7} (2010) 1993-1995.
14. V. R. Kulli. On Banhatti-Sombor indices.International Journal of Applied Chemistry,8(1)(2021), 21-25

* * * * * * * * * *